



Calculation of predictions for non-identical particle correlations in heavy ions collisions at LHC energies from hydrodynamics-inspired models

MASTER OF SCIENCE THESIS

Author:
Mateusz Wojciech Gałażyn

Supervisor:
Prof. Adam Kisiel

Warsaw, 14th November 2014



Wyznaczenie przewidywań teoretycznych dla korelacji cząstek nieidentycznych w zderzeniach ciężkich jonów przy energiach LHC w modelach opartych na hydrodynamice

PRACA MAGISTERSKA

Autor:
Mateusz Wojciech Gałażyn

Promotor:
dr hab. inż. Adam Kisiel, prof. PW

Warszawa, 14 listopada 2014

Abstract

Streszczenie

³ Contents

⁴	Introduction	1
⁵	1 Theory of heavy ion collisions	3
⁶	1.1 The Standard Model	3
⁷	1.2 Quantum Chromodynamics	4
⁸	1.2.1 Quarks and gluons	4
⁹	1.2.2 Quantum Chromodynamics potential	5
¹⁰	1.2.3 The quark-gluon plasma	7
¹¹	1.3 Relativistic heavy ion collisions	8
¹²	1.3.1 Stages of heavy ion collision	8
¹³	1.3.2 QGP signatures	10
¹⁴	2 Therminator model	18
¹⁵	2.1 (3+1)-dimensional viscous hydrodynamics	18
¹⁶	2.2 Statistical hadronization	19
¹⁷	2.2.1 Cooper-Frye formalism	20
¹⁸	3 Particle interferometry	22
¹⁹	3.1 HBT interferometry	22
²⁰	3.2 Theoretical approach	23
²¹	3.2.1 Conventions used	23
²²	3.2.2 Two particle wave function	24
²³	3.2.3 Source emission function	25
²⁴	3.2.4 Theoretical correlation function	27
²⁵	3.2.5 Spherical harmonics decomposition of a correlation function	28
²⁶	3.3 Experimental approach	29
²⁷	3.4 Scaling of femtoscopic radii	30
²⁸	3.4.1 Scaling in LCMS	31
²⁹	3.4.2 Scaling in PRF	31
³⁰	4 Results	33
³¹	4.1 Identical particles correlations	33
³²	4.1.1 Spherical harmonics components	33
³³	4.1.2 Centrality dependence of a correlation function	37

34	4.1.3 k_T dependence of a correlation function	38
35	4.2 Results of the fitting procedure	39
36	4.2.1 The three-dimensional femtoscopic radii scaling	39
37	4.2.2 Scaling of one-dimensional radii	43
38	4.3 Discussion of the results	44
39	Conclusions	45

⁴⁰ Introduction

41 Many people were trying to discover what was before the universe which we
42 observe today. Through the years there were appearing more or less successful
43 theories which were trying to describe its origin and behaviour. Among them
44 is one model, which provides a comprehensive explanation for a broad range
45 of phenomena, including the cosmic microwave background, abundance of the
46 light elements and Hubble's law. This model is called The Big Bang theory and
47 has born in the 1927 on the basis of principles proposed by the Belgian priest and
48 scientist Georges Lemaître. Using this model and known laws of physics one can
49 calculate the characteristics of the universe in detail back in time to the extreme
50 densities and temperatures. However, at some point these calculations fail. The
51 extrapolation of the expansion of universe backwards in time using general re-
52 lativity yields an infinite density and temperature at a finite time in the past. This
53 appearance of singularity is a signal of the breakdown of general relativity. The
54 range of this extrapolation towards singularity is debated - certainly we can go
55 no closer than the end of *Planck epoch* i.e. 10^{-43} s. At this very first era the tem-
56 perature of the universe was so high, that the four fundamental forces - electro-
57 magnetism, gravitation, weak nuclear interaction and strong nuclear interaction
58 - were one fundamental force. Between 10^{-43} s and 10^{-36} s of a lifetime of the
59 universe, there is a *grand unification epoch*, at which forces are starting to separate
60 from each other. From 10^{-36} s to 10^{-12} s lasted *electroweak epoch*, when the strong
61 force separated from the electroweak force. After the electroweak epoch, there
62 was the *quark epoch* in which the universe was a dense "soup" of quarks. During
63 this stage the fundamental forces of gravitation, electromagnetism, strong and
64 weak interactions had taken their present forms. The temperature at this mo-
65 ment was still too high to allow quarks to bind together and form hadrons. At
66 the end of quark era, there was a big freeze-out - when the average energy of
67 particle interactions had fallen below the binding energy of hadrons. This era in
68 which quarks became confined into hadrons is known as the hadron epoch. At
69 this moment the matter had started forming nuclei and atoms, which we observe
70 today.

71 Here arises the question: how we can study the very beginning of the
72 universe? To do this, one should create in a laboratory a system with a such
73 large density and high temperature to recreate those conditions. Today, this is
74 achievable through sophisticated machines, which are particle accelerators. In

75 the particle accelerators, like the Large Hadron Collider at CERN, Geneva or
76 Relativistic Heavy Ion Collider at Brookhaven National Laboratory in Upton,
77 New York, the heavy ions after being accelerated to the near speed of light are
78 collided in order to generate extremely dense and hot phase of matter and
79 recreate the quark-gluon plasma. The plasma is believed to behave like an
80 almost ideal fluid and to become a medium, that can be described by the laws of
81 relativistic hydrodynamics.

82 This thesis is a verification of predictions for collective behaviour of the
83 quark-gluon plasma coming from the hydrodynamic equations using the
84 experimental-like analysis for the high energy Pb-Pb collisions generated using
85 the THERMINATOR model.

86 The 1st chapter is an introduction to the theory of heavy ion collisions. It
87 contains the brief description of the Standard Model and Quantum Chromody-
88 namics. The quark-gluon plasma and its signatures are also characterized.

89 In the 2nd chapter there is a description of the relativistic hydrodynamic
90 framework and the THERMINATOR model used to perform the simulations of col-
91 lisions.

92 The 3rd chapter covers the particle interferometry method used in this work.
93 The algorithm of building experimental correlation functions and effects coming
94 from the hydrodynamics in the experimental results for particle interferometry
95 are also presented.

96 In the 4th chapter there is a detailed analysis of the results for two-particle
97 femtoscopy for different pairs of particles. The quantitative analysis of calcu-
98 lated femtoscopic radii as well as the appearance of transverse mass scaling is
99 discussed.

100 Chapter 1

101 Theory of heavy ion collisions

102 1.1 The Standard Model

103 In the 1970s, a new theory of fundamental particles and their interaction
104 emerged. A new concept, which concerns the electromagnetic, weak and strong
105 nuclear interactions between known particles. This theory is called *The Standard
106 Model*. There are seventeen named particles in the standard model, organized
107 into the chart shown below (Fig. 1.1). Fundamental particles are divided into
two families: *fermions* and *bosons*.

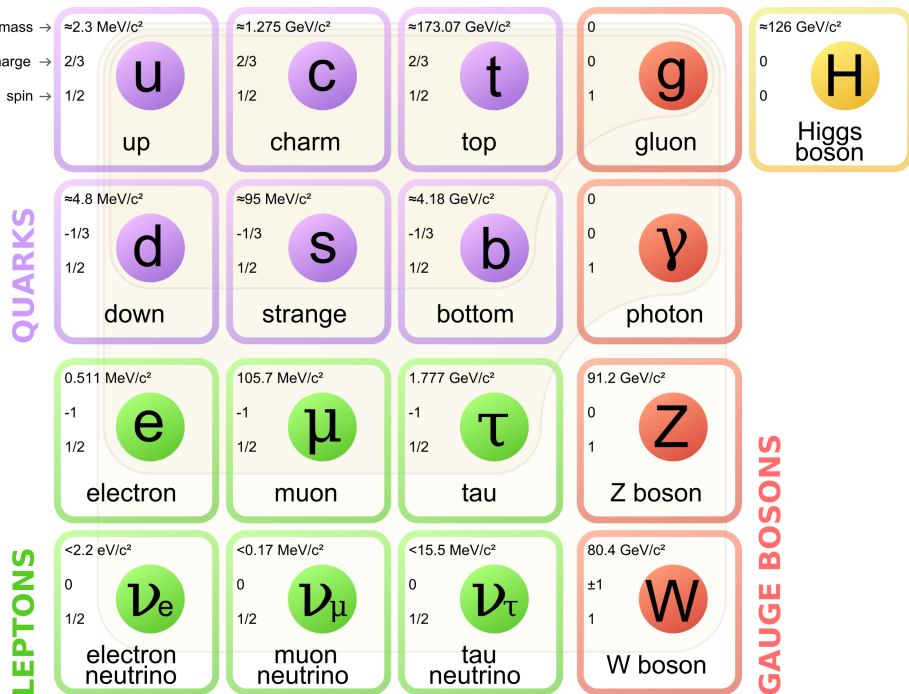


Figure 1.1: The Standard Model of elementary particles [1].

108 Fermions are the building blocks of matter. They are divided into two groups.
 109 Six of them, which must bind together are called *quarks*. Quarks are known to
 110 bind into doublets (*mesons*), triplets (*baryons*) and recently confirmed four-quark
 111 states.¹ Two of baryons, with the longest lifetimes, are forming a nucleus: a pro-
 112 ton and a neutron. A proton is build from two up quarks and one down, and
 113 neutron consists of two down quarks and one up. A proton is found to be a stable
 114 particle (at least it has a lifetime larger than 10^{35} years) and a free neutron has a
 115 mean lifetime about 8.8×10^2 s. Fermions, that can exist independently are called
 116 *leptons*. Neutrinos are a subgroup of leptons, which are only influenced by weak
 117 interaction. Fermions can be divided into three generations (three columns in
 118 the Figure 1.1). Generation I particles can combine into hadrons with the longest
 119 life spans. Generation II and III consists of unstable particles which form also
 120 unstable hadrons.

121 Bosons are force carriers. There are four fundamental forces: weak - respons-
 122 ible for radioactive decay, strong - coupling quarks into hadrons, electromagnetic
 123 - between charged particles and gravity - the weakest, which causes the attraction
 124 between particles with a mass. The Standard Model describes the first three. The
 125 weak force is mediated by W^\pm and Z^0 bosons, electromagnetic force is carried by
 126 photons γ and the carriers of a strong interaction are gluons g . The fifth boson is
 127 a Higgs boson which is responsible for giving other particles mass.

128 1.2 Quantum Chromodynamics

129 1.2.1 Quarks and gluons

130 Quarks interact with each other through the strong interaction. The mediator
 131 of this force is a *gluon* - a massless and chargeless particle. In the quantum chro-
 132 modynamics (QCD) - theory describing strong interaction - there are six types of
 133 "charges" (like electrical charges in the electrodynamics) called *colours*. The col-
 134 ours were introduced because some of the observed particles, like Δ^- , Δ^{++} and
 135 Ω^- appeared to consist of three quarks with the same flavour (ddd , uuu and sss
 136 respectively), which was in conflict with the Pauli principle. One quark can carry
 137 one of the three colours (usually called *red*, *green* and *blue*) and antiquark one of
 138 the three anti-colours respectively. Only colour-neutral (or white) particles could
 139 exist. Mesons are assumed to be a colour-anticolour pair, while baryons are *red-*
 140 *green-blue* triplets. Gluons also are colour-charged and there are 8 types of gluons.
 141 Therefore they can interact with themselves [3].

¹The LHCb experiment at CERN in Geneva confirmed recently existence of $Z(4430)$ - a particle consisting of four quarks [2].

142 **1.2.2 Quantum Chromodynamics potential**

143 As a result of that gluons are massless, one can expect, that the static potential
 144 in the QCD will have the similar form like one in the electrodynamics e.g. $\sim 1/r$
 145 (through an analogy to photons). In reality the QCD potential is assumed to have
 146 the form of [3]

$$V_s = -\frac{4}{3} \frac{\alpha_s}{r} + kr, \quad (1.1)$$

147 where the α_s is a coupling constant of the strong force and the kr part is related
 148 with the *confinement*. In comparison to the electromagnetic force, a value of the
 149 strong coupling constant is $\alpha_s \approx 1$ and the electromagnetic one is $\alpha = 1/137$.

150 The fact that quarks does not exist separately, but they are always bound,
 151 is called a confinement. As two quarks are pulled apart, the linear part kr in
 152 the Eq. 1.1 becomes dominant and the potential becomes proportional to the dis-
 153 tance. This situation resembles stretching of a string. At some point, when the
 154 string is so large it is energetically favourable to create a quark-antiquark pair. At
 155 this moment such pair (or pairs) is formed, the string breaks and the confinement
 is preserved (Fig. 1.2).

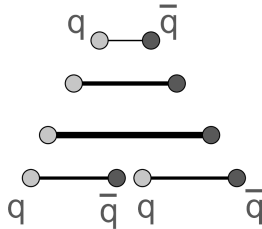


Figure 1.2: A string break and a creation of a pair quark-anti-quark [4].

156 On the other hand, for the small r , an interaction between the quarks and
 157 gluons is dominated by the Coulomb-like term $-\frac{4}{3} \frac{\alpha_s}{r}$. The coupling constant α_s
 158 depends on the four-momentum Q^2 transferred in the interaction. This depend-
 159 ence is presented in Fig. 1.3. The value α_s decreases with increasing momentum
 160 transfer and the interaction becomes weak for large Q^2 , i.e. $\alpha_s(Q) \rightarrow 0$. Be-
 161 cause of weakening of coupling constant, quarks at large energies (or small dis-
 162 tances) are starting to behave like free particles. This phenomenon is known as
 163 an *asymptotic freedom*. The QCD potential has also temperature dependence - the
 164 force strength “melts” with the temperature increase. Therefore the asymptotic
 165 freedom is expected to appear in either the case of high baryon densities (small
 166 distances between quarks) or very high temperatures. This temperature depend-
 167 ence is illustrated in the Fig. 1.4.

168 If the coupling constant α_s is small, one can use perturbative methods to cal-
 169 culate physical observables. Perturbative QCD (pQCD) successfully describes
 170 hard processes (with large Q^2), such as jet production in high energy proton-
 171 antiproton collisions. The applicability of pQCD is defined by the *scale parameter*

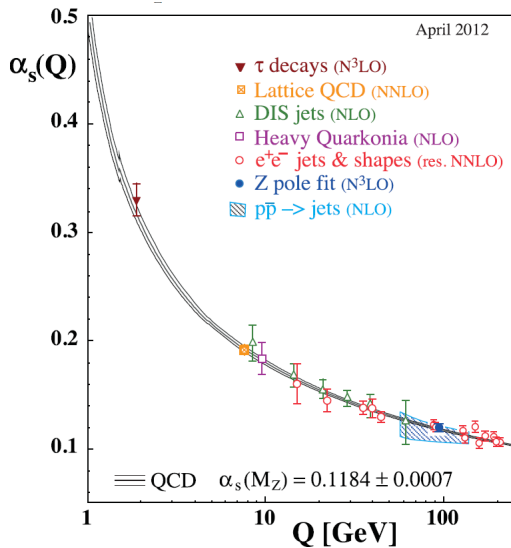


Figure 1.3: The coupling parameter α_s dependence on four-momentum transfer Q^2 [5].

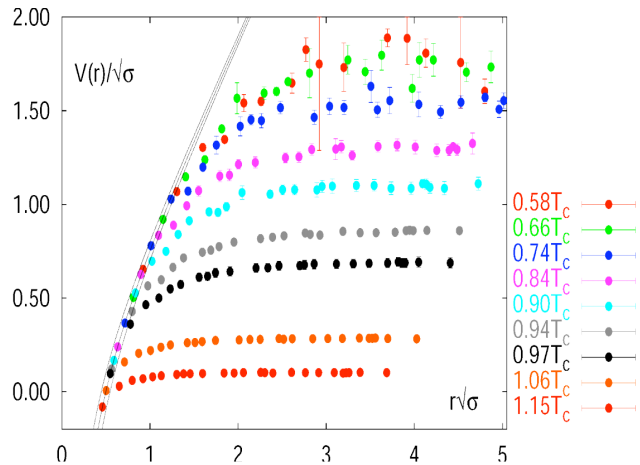


Figure 1.4: The QCD potential for a pair quark-antiquark as a function of distance for different temperatures. A value of a potential decreases with the temperature [4].

¹⁷³ $\Lambda_{QCD} \approx 200$ MeV. If $Q \gg \Lambda_{QCD}$ then the process is in the perturbative domain
¹⁷⁴ and can be described by pQCD. A description of soft processes (when $Q < 1$ GeV)
¹⁷⁵ is a problem in QCD - perturbative theory breaks down at this scale. Therefore,
¹⁷⁶ to describe processes with low Q^2 , one has to use alternative methods like Lattice
¹⁷⁷ QCD. Lattice QCD (LQCD) is non-perturbative implementation of a field theory
¹⁷⁸ in which QCD quantities are calculated on a discrete space-time grid. LQCD al-

lows to obtain properties of matter in equilibrium, but there are some limitations. Lattice QCD requires fine lattice spacing to obtain precise results - therefore large computational resources are necessary. With the constant growth of computing power this problem will become less important. The second problem is that lattice simulations are possible only for baryon density $\mu_B = 0$. At $\mu_B \neq 0$, Lattice QCD breaks down because of the sign problem [6].

1.2.3 The quark-gluon plasma

The new state of matter in which quarks are no longer confined is known as a *quark-gluon plasma* (QGP). The predictions coming from the discrete space-time Lattice QCD calculations reveal a phase transition from the hadronic matter to the quark-gluon plasma at the high temperatures and baryon densities. The res-

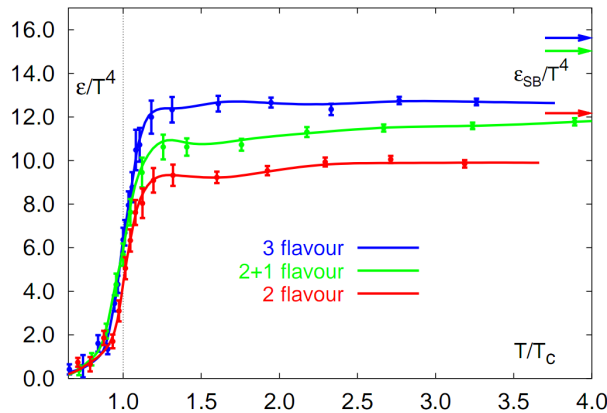


Figure 1.5: A number of degrees of freedom as a function of a temperature [7].

ults obtained from such calculations are shown on Fig. 1.5. The energy density ϵ which is divided by T^4 is a measure of number of degrees of freedom in the system. One can observe significant rise of this value, when the temperature increases past the critical value T_C . Such increase is signaling a phase transition - the formation of QGP [8]. The values of the energy densities plotted in Fig. 1.5 do not reach the Stefan-Boltzmann limit ϵ_{SB} (marked with arrows), which corresponds to an ideal gas. This can indicate some residual interactions in the system. According to the results from the RHIC², the new phase of matter behaves more like an ideal fluid, than like a gas [9].

One of the key questions, to which current heavy ion physics tries to find an answer is the value of a critical temperature T_C as a function of a baryon chemical potential μ_B (baryon density), where the phase transition occur. The results coming from the Lattice QCD are presented in the Fig. 1.6. The phase of matter in which quarks and gluons are deconfined is expected to exist at large

²Relativistic Heavy Ion Collider at Brookhaven National Laboratory in Upton, New York

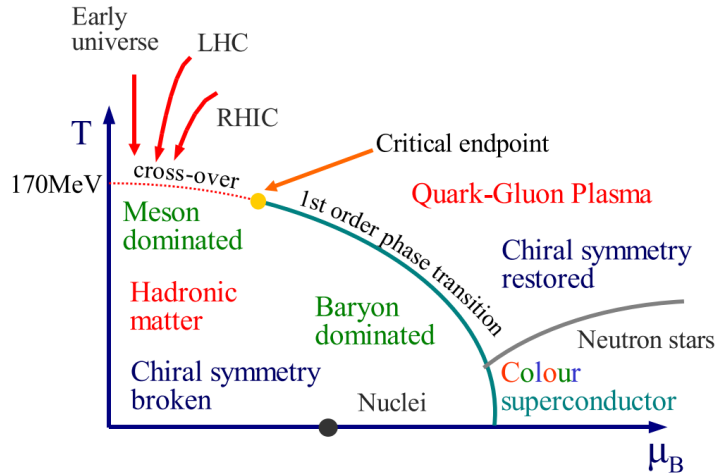


Figure 1.6: Phase diagram coming from the Lattice QCD calculations [8].

temperatures. In the region of small temperatures and high baryon densities, a different state is supposed to appear - a *colour superconductor*. The phase transition between hadronic matter and QGP is thought to be of 1st order at $\mu_B \gg 0$. However as $\mu_B \rightarrow 0$ quarks' masses become significant and a sharp transition transforms into a rapid but smooth cross-over. It is believed that in Pb-Pb collisions observed at the LHC³, the created matter has high enough temperature to be in the quark-gluon plasma phase, then cools down and converts into hadrons, undergoing a smooth transition [8].

1.3 Relativistic heavy ion collisions

1.3.1 Stages of heavy ion collision

To create the quark-gluon plasma one has to achieve high enough temperatures and baryon densities. Such conditions can be recreated in the heavy ion collisions at the high energies. The left side of the Figure 1.7 shows simplified picture of a central collision of two highly relativistic nuclei in the centre-of-mass reference frame. The colliding nuclei are presented as thin disks because of the Lorentz contraction. In the central region, where the energy density is the highest, a new state of matter - the quark-gluon plasma - is supposedly created. Afterwards, the plasma expands ad cools down, quarks combine into hadrons and their mutual interactions cease when the system reaches the *freeze-out* temperature. Subsequently, produced free hadrons move towards the detectors.

On the right side of the Figure 1.7 there is presented a space-time evolution of a collision process, plotted in the light-cone variables (z, t). The two highly

³Large Hadron Collider at CERN, Geneva

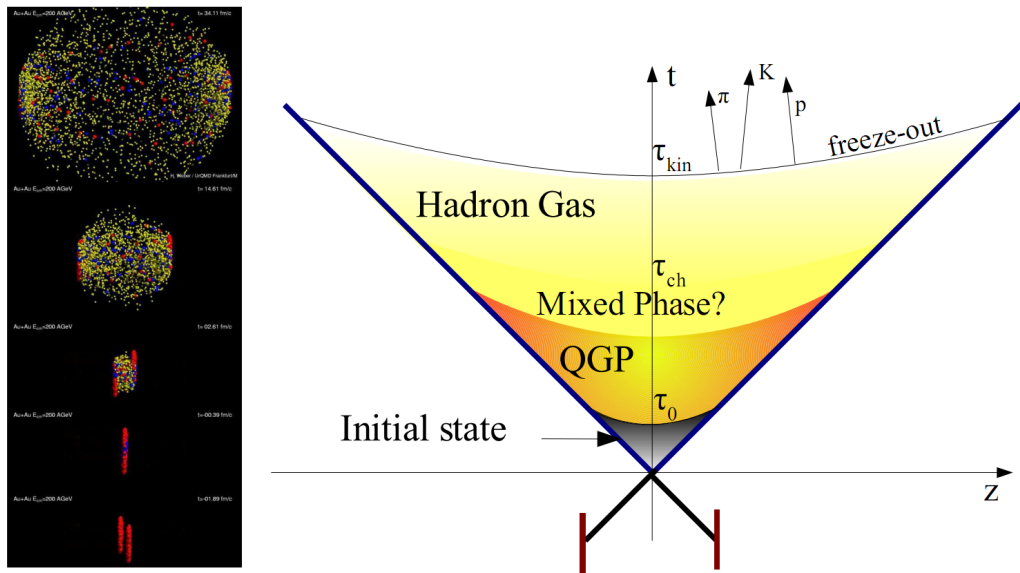


Figure 1.7: Left: stages of a heavy ion collision simulated in the UrQMD model. Right: schematic view of a heavy ion collision evolution [8].

226 relativistic nuclei are traveling basically along the light cone until they collide
 227 at the centre of diagram. Nuclear fragments emerge from the collision again
 228 along the (forward) light cone, while the matter between fragmentation zones
 229 populates the central region. This hot and dense matter is believed to be in the
 230 state of the quark-gluon plasma. There exist several frameworks to describe this
 231 transition to the QGP phase, for example: QCD string breaking, QCD parton cas-
 232 cades or colour glass condensate evolving into glasma and later into quark-gluon
 233 plasma [10].

234 **String breaking** – In the string picture, the nuclei pass through each other forming
 235 colour strings. This is analogous to the situation depicted in the Fig 1.2 - the
 236 colour string is created between quarks inside particular nucleons in nuclei. In
 237 the next step strings decay / fragment forming quarks and gluons or directly
 238 hadrons. This approach becomes invalid at very high energies, when the strings
 239 overlap and cannot be treated as independent objects.

240 **Parton cascade** – The parton⁴ cascade model is based on the pQCD. The col-
 241 liding nuclei are treated as clouds of quarks and which penetrate through each
 242 other. The key element of this method is the time evolution of the parton phase-
 243 space distributions, which is governed by a relativistic Boltzmann equation with
 244 a collision term that contains dominant perturbative QCD interations. The bot-
 245 tleneck of the parton cascade model is the low energies regime, where the Q^2 is
 246 too small to be described by the perturbative theory.

⁴A parton is a common name for a quark and a gluon.

247 **Colour glass condensate** – The colour glass condensate assumes, that the had-
 248 ron can be viewed as a tightly packed system of interacting gluons. The sat-
 249 uration of gluons increases with energy, hence the total number of gluons may
 250 increase without the bound. Such a saturated and weakly coupled gluon system
 251 is called a colour glass condensate. The fast gluons in the condensate are Lorentz
 252 contracted and redistributed on the two very thin sheets representing two col-
 253 liding nuclei. The sheets are perpendicular to the beam axis. The fast gluons
 254 produce mutually orthogonal colour magnetic and electric fields, that only ex-
 255 ist on the sheets. Immediately after the collision, i.e. just after the passage of
 256 the two gluonic sheets after each other, the longitudinal electric and magnetic
 257 fields are produced forming the *glasma*. The glasma fields decay through the
 258 classical rearrangement of the fields into radiation of gluons. Also decays due to
 259 the quantum pair creations are possible. In this way, the quark-gluon plasma is
 260 produced.

261 Interactions within the created quark-gluon plasma bring the system into the
 262 local statistical equilibrium, hence its further evolution can be described by the
 263 relativistic hydrodynamics. The hydrodynamic expansion causes that the sys-
 264 tem becomes more and more dilute. The phase transition from the quark-gluon
 265 plasma to the hadronic gas occurs. Further expansion causes a transition from the
 266 strongly interaction hadronic gas to weakly interacting system of hadrons which
 267 move freely to the detectors. Such decoupling of hadrons is called the *freeze-out*.
 268 The freeze-out can be divided into two phases: the chemical freeze-out and the
 269 thermal one. The *chemical freeze-out* occurs when the inelastic collisions between
 270 constituents of the hadron gas stop. As the system evolves from the chemical
 271 freeze-out to the thermal freeze-out the dominant processes are elastic collisions
 272 (such as, for example $\pi + \pi \rightarrow \rho \rightarrow \pi + \pi$) and strong decays of heavier reso-
 273 nances which populate the yield of stable hadrons. The *thermal freeze-out* is the
 274 stage of the evolution of matter, when the strongly coupled system transforms
 275 to a weakly coupled one (consisting of essentially free particles). In other words
 276 this is the moment, where the hadrons practically stop to interact. Obviously, the
 277 temperatures corresponding to the two freeze-outs satisfy the condition

$$T_{chem} > T_{therm}, \quad (1.2)$$

278 where T_{chem} (inferred from the ratios of hadron multiplicities) is the temperature
 279 of the chemical freeze-out, and T_{therm} (obtained from the investigation of the
 280 transverse-momentum spectra) is the temperature of the thermal freeze-out [10].

281 1.3.2 QGP signatures

282 The quark-gluon plasma is a very short living and unstable state of matter.
 283 One cannot investigate the properties of a plasma and confirm its existence dir-
 284 ectly. Hence, the several experimental effects were proposed as QGP signatures,
 285 some of them have been already observed in heavy ion experiments [8]. As mat-
 286 ter created in the heavy ions collisions is supposed to behave like a fluid, one

should expect appearance of collective behaviour at small transverse momenta - so called *elliptic flow* and *radial flow*. The next signal is the temperature range obtained from the measurements of *direct photons*, which gives us information, that the system created in heavy ion collisions is far above the critical temperature obtained from the LQCD calculations. The *puzzle in the di-lepton spectrum* can be explained by the modification of spectral shape of vector mesons (mostly ρ meson) in the presence of a dense medium. This presence of a medium can also shed light on the *jet quenching* phenomenon - the suppression occurrence in the high p_T domain.

Elliptic flow

In a non-central heavy ion collisions, created region of matter has an almond shape with its shorter axis in the *reaction plane* (Fig. 1.8). The pressure gradient is much larger in-plane rather than out-of-plane. This causes larger acceleration and transverse velocities in-plane rather than out-of-plane. Such differences can

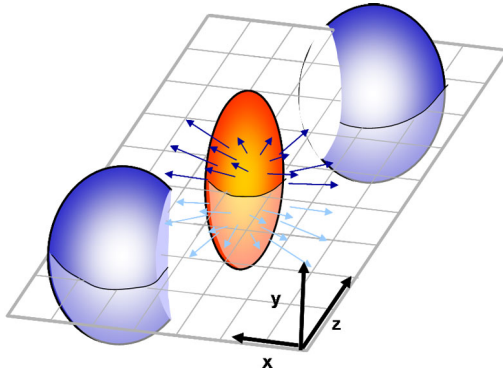


Figure 1.8: Overlapping region which is created in heavy ion collisions has an almond shape. Visible x-z plane is a *reaction plane*. The x-y plane is a *transverse plane*. The z is a direction of the beam [11].

be investigated by studying the distribution of particles with respect to the reaction plane orientation [12]:

$$E \frac{d^3 N}{dp^3} = \frac{1}{2\pi} \frac{d^2 N}{p_T dp_T dy} (1 + 2v_1 \cos(\phi) + 2v_2 \cos(2\phi) + \dots), \quad (1.3)$$

where ϕ is the angle between particle transverse momentum p_T (a momentum projection on a transverse plane) and the reaction plane, N is a number of particles and E is an energy of a particle. The y variable is a *rapidity* defined as:

$$y = \frac{1}{2} \ln \left(\frac{E + p_L}{E - p_L} \right), \quad (1.4)$$

306 where p_L is a longitudinal component of a momentum (parallel to the beam direction).
 307 The v_n coefficients indicate the shape of a system. For the most central collisions
 308 ($b = 0$ - see Fig. 1.9) all coefficients vanish $\bigwedge_{n \in N_+} v_n = 0$ (the overlapping region has the spherical shape). The Fourier series elements in the parentheses

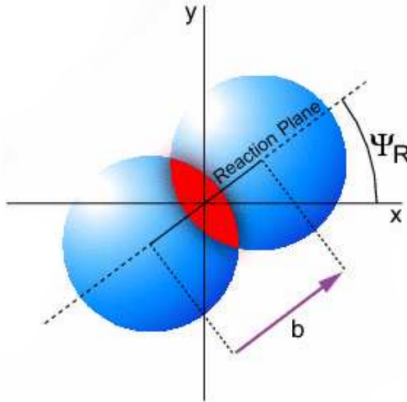


Figure 1.9: Cross-section of a heavy ion collision in a transverse plane. Ψ_R is an angle between transverse plane and the reaction plane. The b parameter is an *impact parameter* - a distance between centers of nuclei during a collision. An impact parameter is related with the centrality of a collision and a volume of the quark-gluon plasma [12].

309 in Eq. 1.3 represent different kinds of a flow. The first value: "1" represents the
 310 *radial flow* - an isotropic flow in every direction. Next coefficient v_1 is responsible
 311 for *direct flow*. The v_2 coefficient is a measure of elliptic anisotropy (*elliptic flow*).
 312 The v_2 has to build up in the early stage of a collision - later the system becomes
 313 too dilute: space asymmetry and the pressure gradient vanish. Therefore the
 314 observation of elliptic flow means that the created matter was in fact a strongly
 315 interacting matter.

316 The v_2 coefficient was measured already at CERN SPS, LHC and RHIC. For
 317 the first time hydrodynamics successfully described the collision dynamics as the
 318 measured v_2 reached hydrodynamic limit (Fig. 1.10). As expected, there is a mass
 319 ordering of v_2 as a function of p_T (lower plot in the Fig. 1.10) with pions having
 320 the largest and protons the smallest anisotropy. In the upper plots in the Fig. 1.10
 321 there is a v_2 as a function of transverse kinetic energy. The left plot shows the
 322 two universal trend lines for baryons and mesons. After the scaling of v_2 and the
 323 kinetic energy by the number of valence quarks, all of the hadrons follow the
 324 same universal curve. Those plots show that strong collectivity is observed in
 325 heavy ion collisions.

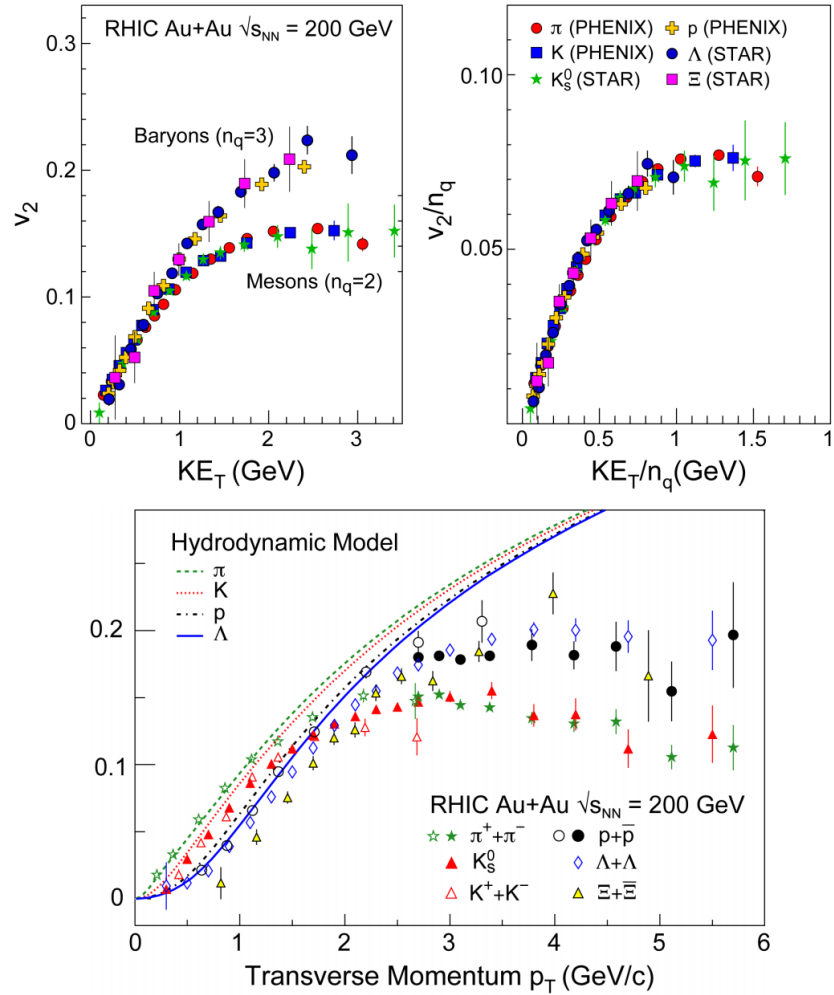


Figure 1.10: *Lower:* The elliptic flow v_2 follows the hydrodynamical predictions for an ideal fluid perfectly. Note that > 99% of all final hadrons have $p_T < 1.5$ GeV/c. *Upper left:* The v_2 plotted versus transverse kinetic energy $KE_T = m_T - m_0 = \sqrt{p_T^2 + m_0^2} - m_0$. The v_2 follows different universal curves for mesons and baryons. *Upper right:* When scaled by the number of valence quarks, the v_2 follows the same universal curve for all hadrons and for all values of scaled transverse kinetic energy [13].

327 Transverse radial flow

328 Elliptic flow described previously is caused by the pressure gradients which
 329 must also produce a more simple collective behaviour of matter - a movement
 330 inside-out, called radial flow. Particles are pushed to higher momenta and they
 331 move away from the center of the collision. A source not showing collective

332 behaviour, like pp collisions, produces particle spectra that can be fitted by a
 333 power-law [8]:

$$\frac{1}{2\pi p_T} \frac{d^2N}{dp_T d\eta} = C \left(1 + \frac{p_T}{p_0} \right)^{-\gamma}. \quad (1.5)$$

334 The η variable is a *pseudorapidity* defined as follows:

$$\eta = \frac{1}{2} \ln \left(\frac{p + p_L}{p - p_L} \right) = -\ln \left(\frac{\theta}{2} \right), \quad (1.6)$$

where θ is an emission angle $\cos \theta = p_L/p$.

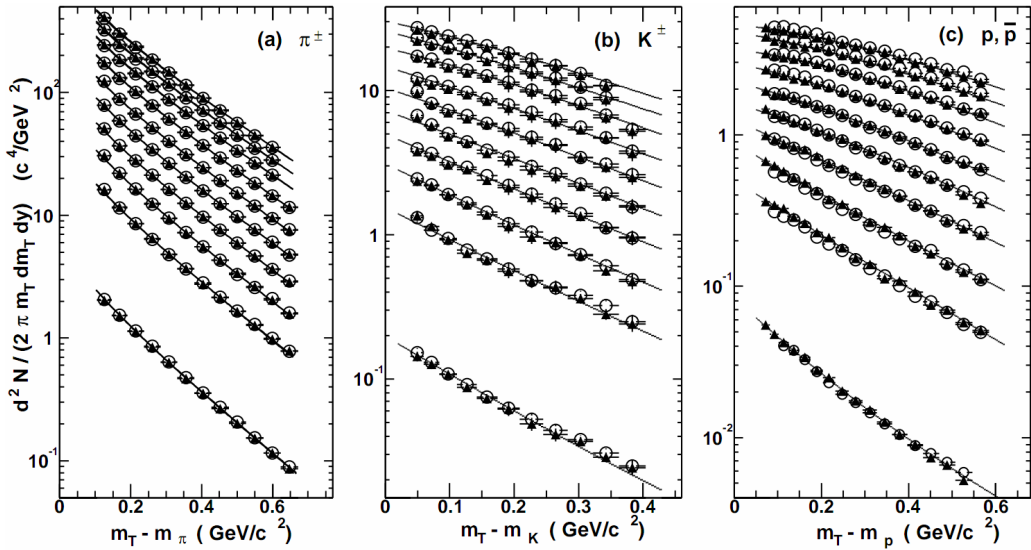


Figure 1.11: Invariant yield of particles versus transverse mass $m_T = \sqrt{p_T^2 + m_0^2}$ for π^\pm , K^\pm , p and \bar{p} at mid-rapidity for p+p collisions (bottom) and Au+Au events from 70-80% (second bottom) to 0-5% (top) centrality [14].

335
 336 The hydrodynamical expansion of a system gives the same flow velocity kick
 337 for different kind of particles - ones with bigger masses will gain larger p_T boost.
 338 This causes increase of the yield of particles with larger transverse momenta. In
 339 the invariant yield plots one can observe the decrease of the slope parameter,
 340 especially for the heavier hadrons. This is presented in the Fig. 1.11. The most
 341 affected spectra are ones of kaons (b) and protons (c). One can notice decrease
 342 of the slope parameter for heavy ion collisions (plots from second bottom to top)
 343 comparing to the proton-proton collisions (bottom ones), where no boost from
 344 radial flow should occur [8].

345 Direct photons

346 The direct photons are photons, which are not coming from the final state
 347 hadrons decays. Their sources can be various interaction from charged particles

348 created in the collision, either at the partonic or at the hadronic level. Direct
 349 photons are considered to be an excellent probe of the early stage of the collision.
 350 This is because their mean free path is very large to the created system in the
 351 collision. Thus photons created at the early stage leave the system without suf-
 352 fering any interaction and retain information about this stage, in particular about
 353 its temperature.

354 One can distinguish two kinds of direct photons: *thermal* and *prompt*. Thermal
 355 photons can be emitted from the strong processes in the quark-gluon plasma in-
 356 volving quarks and gluons or hot hadronic matter (e.g. processes: $\pi\pi \rightarrow \rho\gamma$,
 357 $\pi\rho \rightarrow \pi\gamma$). Thermal photons can be observed in the low p_T region. Prompt
 358 photons are believed to come from “hard” collisions of initial state partons be-
 359 longing to the colliding nuclei. The prompt photons can be described using the
 360 pQCD. They will dominate the high p_T region. The analysis of transverse mo-
 361 mentum of spectra of direct photons revealed, that the temperature of the source
 362 of thermal photons produced in heavy ion collisions at RHIC is in the range 300-
 363 600 MeV (Fig. 1.12). Hence the direct photons had to come from a system whose
 temperature is far above from the critical temperature for QGP creation.

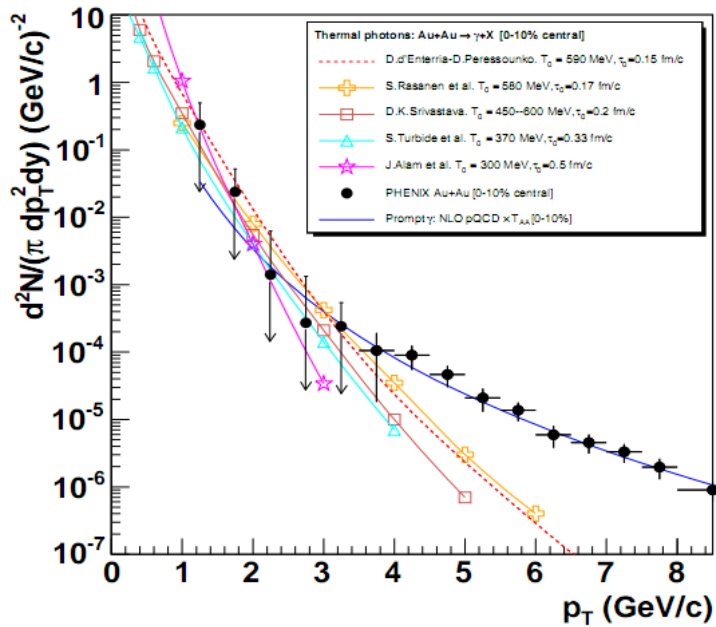


Figure 1.12: Thermal photons spectra for the central Au+Au collisions at $\sqrt{s_{NN}} = 200 \text{ GeV}$ at computed within different hydrodynamical models compared with the pQCD calculations (solid line) and experimental data from PHENIX (black dots) [15].

365 **Puzzle in di-lepton mass spectrum**

366 The invariant mass spectra (Fig. 1.13) of lepton pairs reveal many peaks cor-
 367 responding to direct decays of various mesons into a lepton pair. The continu-
 368 ous background in this plot is caused by the decays of hadrons into more than
 369 two leptons (including so-called *Dalitz decays* into a lepton pair and a photon).
 Particular hadron decay channels, which contribute to this spectrum are shown

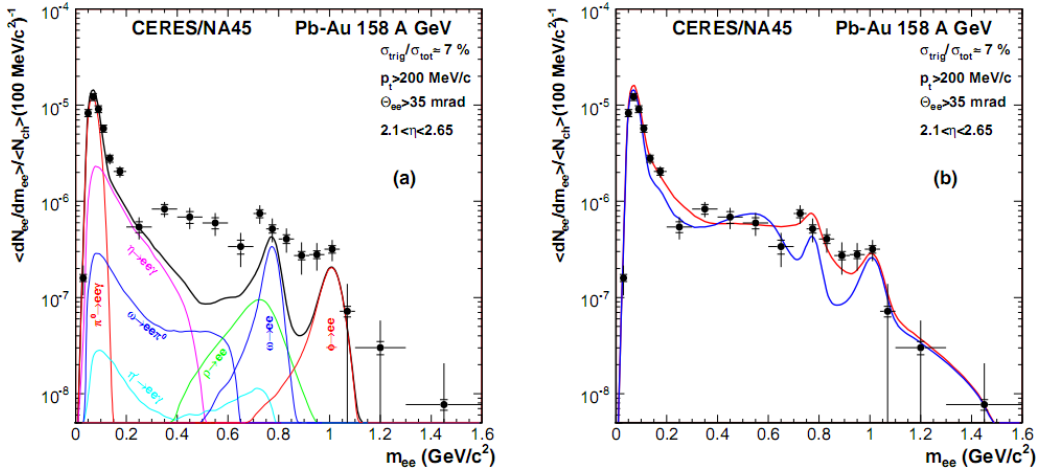


Figure 1.13: Left: Invariant mass spectrum of $e^+ - e^-$ pairs in $\text{Pb} + \text{Au}$ collisions at 158A GeV compared to the sum coming from the hadron decays predictions. Right: The expectations coming from model calculations assuming a dropping of the ρ mass (blue) or a spread of the ρ width in the medium [16].

370 in the Fig. 1.13 with the coloured lines and their sum with the black one. The
 371 sum (called *the hadronic cocktail*) of various components describes experimental
 372 spectra coming from the simple collisions (like $p + p$ or $p + A$) quite well with the
 373 statistical and systematical uncertainties [9]. This situation is different consider-
 374 ing more complicated systems i.e. $A + A$. Spectra coming from $\text{Pb} + \text{Au}$ collisions
 375 are presented on the plots in the Fig. 1.13. The “hadronic cocktail” does not de-
 376 scribe the data, in the mass range between the π and the ρ mesons a significant
 377 excess of electron pairs over the calculated sum is observed. Theoretical expla-
 378 nation of this phenomenon assumes modification of the spectral shape of vector
 379 mesons in a dense medium. Two different interpretations of this increase were
 380 proposed: a decrease of meson mass with the medium density and increase of the
 381 meson width in the dense medium. In principle, one could think of simultaneous
 382 occurrence of both effects: mass shift and resonance broadening. Experimental
 383 results coming from the CERES disfavour the mass shift hypothesis indicating
 384 only broadening of resonance peaks (Fig. 1.13b) [9].

386 **Jet quenching**

387 A jet is defined as a group of particles with close vector momenta and high en-
 388 ergies. It has its beginning when the two partons are going in opposite directions
 389 and have energy big enough to produce new quark-antiquark pair and then ra-
 390 diate gluons. This process can be repeated many times and it results in two back-
 391 to-back jets of hadrons. It has been found that jets in the opposite hemisphere
 392 (*away-side jets*) show a very different pattern in d+Au and Au+Au collisions. This
 393 is shown in the azimuthal correlations in the Fig. 1.14. In d+Au collisions, like in
 394 p+p, a pronounced away-side jet appears around $\Delta\phi = \pi$, exactly opposite to the
 395 trigger jet, what is typical for di-jet events. In central Au+Au collisions the away-
 jet is suppressed. When the jet has its beginning near the surface of the quark-

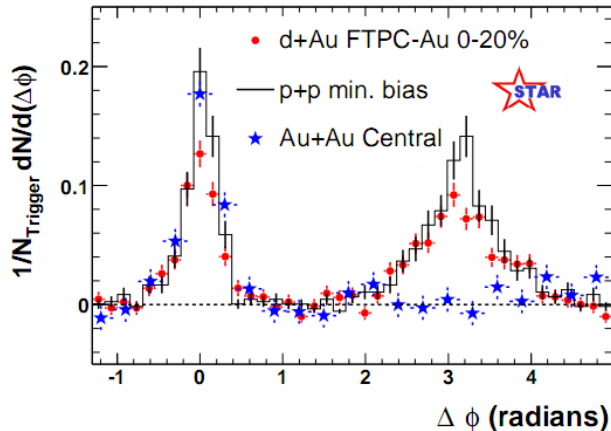


Figure 1.14: Azimuthal angle difference $\Delta\phi$ distributions for different colliding systems at $\sqrt{s_{NN}} = 200$ GeV. Transverse momentum cut: $p_T > 2$ GeV. For the Au+Au collisions the away-side jet is missing [17].

396
 397 gluon plasma, one of the jets (*near-side jet*) leaves the system almost without any
 398 interactions. This jet is visible on the correlation plot as a high peak at $\Delta\phi = 0$.
 399 However, the jet moving towards the opposite direction has to penetrate a dense
 400 medium. The interaction with the plasma causes energy dissipation of particles
 401 and is visible on an azimuthal correlation plot as disappearance of the away-side
 402 jet [9].

403 **Chapter 2**

404 **Therminator model**

405 THERMINATOR [18] is a Monte Carlo event generator designed to investigate
406 the particle production in the relativistic heavy ion collisions. The functionality
407 of the code includes a generation of the stable particles and unstable resonances
408 at the chosen hypersurface model. It performs the statistical hadronization which
409 is followed by space-time evolution of particles and the decay of resonances. The
410 key element of this method is an inclusion of a complete list of hadronic reso-
411 nances, which contribute very significantly to the observables. The second version
412 of THERMINATOR [19] comes with a possibility to incorporate any shape of freeze-
413 out hypersurface and the expansion velocity field, especially those generated ex-
414 ternally with various hydrodynamic codes.

415 **2.1 (3+1)-dimensional viscous hydrodynamics**

416 Most of the relativistic viscous hydrodynamic calculations are done in
417 (2+1)-dimensions. Such simplification assumes boost-invariance of a matter
418 created in a collision. Experimental data reveals that no boost-invariant region is
419 formed in the collisions [20]. Hence, for the better description of created system
420 a (3+1)-dimensional model is required.

421 In the four dimensional relativistic dynamics one can describe a system
422 using a space-time four-vector $x^\nu = (ct, x, y, z)$, a velocity four-vector
423 $u^\nu = \gamma(c, v_x, v_y, v_z)$ and a energy-momentum tensor $T^{\mu\nu}$. The particular
424 components of $T^{\mu\nu}$ have a following meaning:

- 425 • T^{00} - an energy density,
- 426 • $cT^{0\alpha}$ - an energy flux across a surface x^α ,
- 427 • $T^{\alpha 0}$ - an α -momentum flux across a surface x^α multiplied by c ,
- 428 • $T^{\alpha\beta}$ - components of momentum flux density tensor,

429 where $\gamma = (1 - v^2/c^2)^{-1/2}$ is Lorentz factor and $\alpha, \beta \in \{1, 2, 3\}$. Using u^ν one can
 430 express $T^{\mu\nu}$ as follows [21]:

$$T_0^{\mu\nu} = (e + p)u^\mu u^\nu - pg^{\mu\nu} \quad (2.1)$$

431 where e is an energy density, p is a pressure and $g^{\mu\nu}$ is an inverse metric tensor:

$$g^{\mu\nu} = \begin{bmatrix} 1 & 0 & 0 & 0 \\ 0 & -1 & 0 & 0 \\ 0 & 0 & -1 & 0 \\ 0 & 0 & 0 & -1 \end{bmatrix}. \quad (2.2)$$

432 The presented version of energy-momentum tensor (Eq. 2.1) can be used to de-
 433 scribe dynamics of a perfect fluid. To take into account influence of viscosity,
 434 one has to apply the following corrections coming from shear $\pi^{\mu\nu}$ and bulk Π
 435 viscosities [22]:

$$T^{\mu\nu} = T_0^{\mu\nu} + \pi^{\mu\nu} + \Pi(g^{\mu\nu} - u^\mu u^\nu). \quad (2.3)$$

436 The stress tensor $\pi^{\mu\nu}$ and the bulk viscosity Π are solutions of dynamical equa-
 437 tions in the second order viscous hydrodynamic framework [21]. The compari-
 438 son of hydrodynamics calculations with the experimental results reveal, that the
 439 shear viscosity divided by entropy η/s has to be small and close to the AdS/CFT
 440 estimate $\eta/s = 0.08$ [22, 23]. The bulk viscosity over entropy value used in calcu-
 441 lations is $\zeta/s = 0.04$ [22].

442 When using $T^{\mu\nu}$ to describe system evolving close to local thermodynamic
 443 equilibrium, relativistic hydrodynamic equations in a form of:

$$\partial_\mu T^{\mu\nu} = 0 \quad (2.4)$$

444 can be used to describe the dynamics of the local energy density, pressure and
 445 flow velocity.

446 Hydrodynamic calculations are starting from the Glauber¹ model initial con-
 447 ditions. The collective expansion of a fluid ends at the freeze-out hypersurface.
 448 That surface is usually defined as a constant temperature surface, or equivalently
 449 as a cut-off in local energy density. The freeze-out is assumed to occur at the
 450 temperature $T = 140$ MeV.

451 2.2 Statistical hadronization

452 Statistical description of heavy ion collision has been successfully used
 453 to describe quantitatively *soft* physics, i.e. the regime with the transverse
 454 momentum not exceeding 2 GeV. The basic assumption of the statistical
 455 approach of evolution of the quark-gluon plasma is that at some point of the

¹The Glauber Model is used to calculate “geometrical” parameters of a collision like an impact parameter, number of participating nucleons or number of binary collisions.

space-time evolution of the fireball, the thermal equilibrium is reached. When the system is in the thermal equilibrium the local phase-space densities of particles follow the Fermi-Dirac or Bose-Einstein statistical distributions. At the end of the plasma expansion, the freeze-out occurs. The freeze-out model incorporated in the THERMINATOR model assumes, that chemical and thermal freeze-out occur at the same time.

2.2.1 Cooper-Frye formalism

The result of the hydrodynamic calculations is the freeze-out hypersurface Σ^μ . A three-dimensional element of the surface is defined as [19]

$$d\Sigma_\mu = \epsilon_{\mu\alpha\beta\gamma} \frac{\partial x^\alpha}{\partial \alpha} \frac{\partial x^\beta}{\partial \beta} \frac{\partial x^\gamma}{\partial \gamma} d\alpha d\beta d\gamma, \quad (2.5)$$

where $\epsilon_{\mu\alpha\beta\gamma}$ is the Levi-Civita tensor and the variables $\alpha, \beta, \gamma \in \{1, 2, 3\}$ are used to parametrize the three-dimensional freeze-out hypersurface in the Minkowski four-dimensional space. The Levi-Civita tensor is equal to 1 when the indices form an even permutation (eg. ϵ_{0123}), to -1 when the permutation is odd (e.g. ϵ_{2134}) and has a value of 0 if any index is repeated. Therefore [19],

$$d\Sigma_0 = \begin{vmatrix} \frac{\partial x}{\partial \alpha} & \frac{\partial x}{\partial \beta} & \frac{\partial x}{\partial \gamma} \\ \frac{\partial y}{\partial \alpha} & \frac{\partial y}{\partial \beta} & \frac{\partial y}{\partial \gamma} \\ \frac{\partial z}{\partial \alpha} & \frac{\partial z}{\partial \beta} & \frac{\partial z}{\partial \gamma} \end{vmatrix} d\alpha d\beta d\gamma \quad (2.6)$$

and the remaining components are obtained by cyclic permutations of t, x, y and z .

One can obtain the number of hadrons produced on the hypersurface Σ^μ from the Cooper-Frye formalism. The following integral yields the total number of created particles [19]:

$$N = (2s + 1) \int \frac{d^3 p}{(2\pi)^3 E_p} \int d\Sigma_\mu p^\mu f(p_\mu u^\mu), \quad (2.7)$$

where $f(p_\mu u^\mu)$ is the phase-space distribution of particles (for stable ones and resonances). One can simply derive from Eq. 2.7, the dependence of the momentum density [24]:

$$E \frac{d^3 N}{dp^3} = \int d\Sigma_\mu f(p_\mu u^\mu) p^\mu. \quad (2.8)$$

The momentum distribution f contains non-equilibrium corrections:

$$f = f_0 + \delta f_{shear} + \delta f_{bulk}, \quad (2.9)$$

where

$$f_0(p_\mu u^\mu) = \left\{ \exp \left[\frac{p_\mu u^\mu - (B\mu_B + I_3\mu_{I_3} + S\mu_S + C\mu_C)}{T} \right] \pm 1 \right\}^{-1} \quad (2.10)$$

481 In case of fermions, in the Eq. 2.10 there is a plus sign and for bosons, minus
 482 sign respectively. The thermodynamic quantities appearing in the $f_0(\cdot)$ are T -
 483 temperature, μ_B - baryon chemical potential, μ_{I_3} - isospin chemical potential, μ_S
 484 - strange chemical potential, μ_C - charmed chemical potential and the s is a spin of
 485 a particle. The hydrodynamic calculations yield the flow velocity at freeze-out as
 486 well as the stress and bulk viscosity tensors required to calculate non-equilibrium
 487 corrections to the momentum distribution used in Eq. 2.7. The term coming from
 488 shear viscosity has a form [22]

$$\delta f_{shear} = f_0(1 \pm f_0) \frac{1}{2T^2(e + p)} p^\mu p^\nu \pi_{\mu\nu} \quad (2.11)$$

489 and bulk viscosity

$$\delta f_{bulk} = C f_0(1 \pm f_0) \left(\frac{(u^\mu p_\mu)^2}{3u^\mu p_\mu} - c_s^2 u^\mu p_\mu \right) \Pi \quad (2.12)$$

490 where c_s is sound velocity and

$$\frac{1}{C} = \frac{1}{3} \frac{1}{(2\pi)^3} \sum_{hadrons} \int d^3p \frac{m^2}{E} f_0(1 \pm f_0) \left(\frac{p^2}{3E} - c_s^2 E \right). \quad (2.13)$$

491 The equations presented above are directly used in the THERMINATOR to gen-
 492 erate the primordial hadrons (created during freeze-out) with the Monte-Carlo
 493 method. Resonances produced in this way, propagate and decay, in cascades if
 494 necessary. For every generated particle, its origin point either on a hypersurface
 495 or is associated with the point of the decay of the parent particle. This informa-
 496 tion is kept in the simulation due to its importance for the femtoscopic analysis.

497 **Chapter 3**

498 **Particle interferometry**

499 Two-particle interferometry (also called *femtoscopy*) gives a possibility to
500 investigate space-time characteristics of the particle-emitting source created
501 in heavy ion collisions. Through the study of particle correlations, their
502 momentum distributions can be used to obtain information about the spatial
503 extent of the created system. Using this method, one can measure sizes of the
504 order of 10^{-15} m and time of the order of 10^{-23} s.

505 **3.1 HBT interferometry**

506 In the 1956 Robert Hanbury Brown and Richard Q. Twiss proposed a
507 method which through analysis of interference between photons allowed to
508 investigate angular dimensions of stars. The most important result from the
509 Hanbury-Brown-Twiss experiments is that two indistinguishable particles can
510 produce an interference effect. There is almost no difference between normal
511 interferometry and HBT method, except that the latter one does not take into
512 account information about phase shift of registered particles. At the beginning
513 this method was used in astronomy for photon interference, but this effect can
514 be used also to measure extent of any emitting source. This method was adapted
515 to heavy ion collisions to investigate dimensions of a system created in those
516 collisions by studying correlations of identical particles [25]. The main difference
517 between HBT method in astronomy and femtoscopy is that the first one is based
518 on space-time HBT correlations and the latter one uses momentum correlations.
519 The momentum correlations yield the space-time picture of the source, whereas
520 the space-time HBT correlations provide the characteristic relative momenta of
521 emitted photons, which gives the angular size of the star without the knowledge
522 of its radius and lifetime [10].

523 3.2 Theoretical approach

524 Intensity interferometry in heavy ion physics uses similar mathematical form-
 525 alism as the astronomy HBT measurement. Through the measurement of corre-
 526 lation between particles as a function of their relative momentum one can deduce
 527 the average separation between emitting sources.

528 **3.2.1 Conventions used**

529 In heavy ion collisions to describe particular directions, components of mo-
 530 mentum and location of particles, one uses naming convention called the Bertsch-
 Pratt coordinate system. This system is presented in the Fig. 3.1. The three dir-

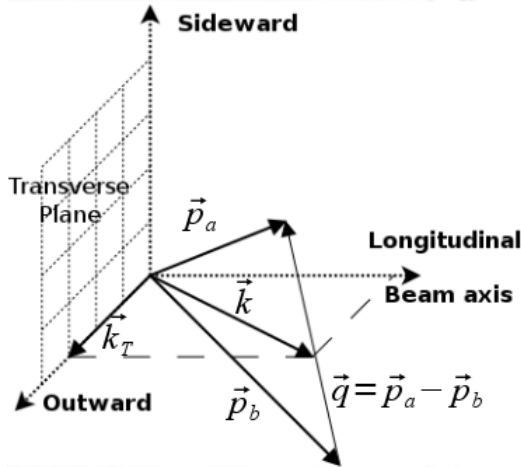


Figure 3.1: Bertsch-Pratt direction naming convention used in heavy ion collision.

531 ections are called *longitudinal*, *outward* and *sideward*. The longitudinal direction
 532 is parallel to the beam axis. The plane perpendicular to the beam axis is called
 533 a *transverse plane*. A projection of a particle pair momentum $\mathbf{k} = (\mathbf{p}_a + \mathbf{p}_b)/2$
 534 on a transverse plane (a *transverse momentum* \mathbf{k}_T) determines *outward* direction:
 535 $(\mathbf{k})_{out} = \mathbf{k}_T$. A direction perpendicular to the longitudinal and outward is called
 536 *sideward*.

537 A particle pair is usually described using two coordinate systems. The first
 538 one, *Longitudinally Co-Moving System* (**LCMS**) is moving along the particle pair
 539 with the longitudinal direction, in other words, the pair longitudinal momentum
 540 vanishes: $(\mathbf{p}_a)_{long} = -(\mathbf{p}_b)_{long}$. The second system is called *Pair Rest Frame* (**PRF**).
 541 In the PRF the centre of mass rests: $\mathbf{p}_a = -\mathbf{p}_b$. Variables which are expressed in
 542 the PRF are marked with a star (e.g. \mathbf{k}^*).

543 The transition of space-time coordinates from LCMS to PRF is simply
 a boost along the outward direction, with the transverse velocity of the

pair $\beta_T = (\mathbf{v}/c)_{out}$ [25]:

$$r_{out}^* = \gamma_t(r_{out} - \beta_T \Delta t) \quad (3.1)$$

$$r_{side}^* = r_{side} \quad (3.2)$$

$$r_{long}^* = r_{long} \quad (3.3)$$

$$\Delta t^* = \gamma_T(\Delta t - \beta_T r_{out}) , \quad (3.4)$$

where $\gamma_T = (1 - \beta_T^2)^{-1/2}$ is the Lorentz factor. However, in calculations performed in this work the equal time approximation is used, which assumes that particles in a pair were produced at the same time in PRF - the Δt^* is neglected.

The most important variables used to describe particle pair are their total momentum $\mathbf{P} = \mathbf{p}_a + \mathbf{p}_b$ and relative momentum $\mathbf{q} = \mathbf{p}_a - \mathbf{p}_b$. In the PRF one has $\mathbf{q} = 2\mathbf{k}^*$, where \mathbf{k}^* is a momentum of the first particle in PRF.

3.2.2 Two particle wave function

Let us consider two identical particles with momenta \mathbf{p}_1 and \mathbf{p}_2 emitted from space points \mathbf{x}_1 and \mathbf{x}_2 . Those emitted particles can be treated as two incoherent waves. If the particles are identical, they are also indistinguishable, therefore one

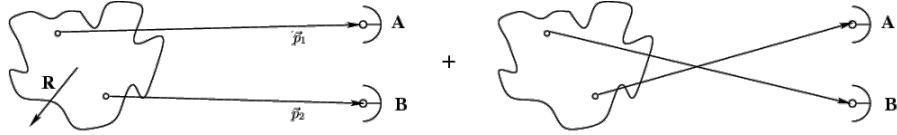


Figure 3.2: The pair wave function is a superposition of all possible states. In case of particle interferometry it includes two cases: particles with momenta p_1, p_2 registered by detectors A, B and p_1, p_2 registered by B, A respectively.

has also take into account the scenario, where the particle with momentum \mathbf{p}_1 is emitted from \mathbf{x}_2 and particle \mathbf{p}_2 from \mathbf{x}_1 (Fig. 3.2). In such case, the wave function describing behaviour of a pair has to contain both components [8]:

$$\Psi_{ab}(\mathbf{q}) = \frac{1}{\sqrt{2}} [\exp(-i\mathbf{p}_1\mathbf{x}_1 - i\mathbf{p}_2\mathbf{x}_2) \pm \exp(-i\mathbf{p}_2\mathbf{x}_1 - i\mathbf{p}_1\mathbf{x}_2)] . \quad (3.5)$$

A two particle wave function of identical bosons is symmetric ("+" sign in Eq. 3.5) and in case of identical fermions - antisymmetric ("−" sign). This anti-symmetrization or symmetrization implies the correlation effect coming from the Fermi-Dirac or Bose-Einstein statistics accordingly.

To provide full description of a system consisting of two charged hadrons, one has to include in the wave function besides quantum statistics also Coulomb and strong Final State Interactions. Considering identical particles systems, the quantum statistics is a main source of a correlation. Hence, in case of space-time analysis of particle emitting source, effects coming from the Coulomb and Strong interactions can be neglected.

567 **3.2.3 Source emission function**

568 To describe particle emitting source, one uses a single emission function [25]:

569

$$S_A(\mathbf{x}_1, \mathbf{p}_1) = \int S(\mathbf{x}_1, \mathbf{p}_1, \mathbf{x}_2, \mathbf{p}_2, \dots, \mathbf{x}_N, \mathbf{p}_N) d\mathbf{x}_2 d\mathbf{p}_2 \dots d\mathbf{x}_N d\mathbf{p}_N \quad (3.6)$$

570 and a two-particle one:

$$S_{AB}(\mathbf{x}_1, \mathbf{p}_1, \mathbf{x}_2, \mathbf{p}_2) = \int S(\mathbf{x}_1, \mathbf{p}_1, \mathbf{x}_2, \mathbf{p}_2, \dots, \mathbf{x}_N, \mathbf{p}_N) d\mathbf{x}_3 d\mathbf{p}_3 \dots d\mathbf{x}_N d\mathbf{p}_N . \quad (3.7)$$

571 Emission function $S(\cdot)$ can be interpreted as a probability to emit a particle, or
 572 a pair of particles from a given space-time point with a given momentum. In
 573 principle, the source emission function should encode all physics aspects of the
 574 particle emission process i.e. the symmetrization for bosons and fermions, as
 575 well as the two-body and many body Final State Interactions. Instead of this,
 576 one assume that each particle's emission process is independent - the interac-
 577 tion between final-state particles after their creation is independent from their
 578 emission process. The assumption of this independence allows to construct two-
 579 particle emission function from single particle emission functions via a convolu-
 580 tion [25]:

$$S(\mathbf{k}^*, \mathbf{r}^*) = \int S_A(\mathbf{p}_1, \mathbf{x}_1) S_B(\mathbf{p}_2, \mathbf{x}_2) \delta \left[\mathbf{k}^* - \frac{\mathbf{p}_1 + \mathbf{p}_2}{2} \right] \delta [\mathbf{r}^* - (\mathbf{x}_1 + \mathbf{x}_2)] \times d^4 \mathbf{x}_1 d^4 \mathbf{x}_2 d^4 \mathbf{x}_1 d^3 \mathbf{p}_1 d^3 \mathbf{p}_2 \quad (3.8)$$

581 In case of identical particles, ($S_A = S_B$) several simplifications can be made.
 582 A convolution of the two same Gaussian distributions is also a Gaussian distri-
 583 bution with σ multiplied by $\sqrt{2}$. Femtoscopy can give information only about
 584 two-particle emission function, but when considering Gaussian distribution as
 585 a source function in Eq. 3.8, one can obtain a σ of a single emission function
 586 from a two-particle emission function. The Eq. 3.8 is not reversible - an inform-
 587 ation about $S_A(\cdot)$ cannot be derived from $S_{AB}(\cdot)$. An exception from this rule
 588 is a Gaussian source function, hence it is often used in femtoscopic calculations.
 589 Considering pairs of identical particles, an emission function is assumed to be
 590 described by the following equation in the Pair Rest Frame [25]:

$$S_{1D}^{PRF}(\mathbf{r}^*) = \exp \left(-\frac{r_{out}^{*2} + r_{side}^{*2} + r_{long}^{*2}}{4R_{inv}^2} \right) . \quad (3.9)$$

To change from the three-dimensional variables to the one-dimensional variable
 one requires introduction of the proper Jacobian r^{*2} .

$$S_{1D}^{PRF}(r^*) = r^{*2} \exp \left(-\frac{r^{*2}}{4R_{inv}^2} \right) . \quad (3.10)$$

591 The “4” in the denominator before the “standard deviation” R_{inv} in the Gaussian
 592 distribution comes from the convolution of the two Gaussian distributions,
 593 which multiplies the R_{inv} by a factor of $\sqrt{2}$.

A more complex form of emission function was used by all RHIC and SPS experiments in identical pion femtoscopy:

$$S_{3D}^{LCMS}(\mathbf{r}) = \exp \left(-\frac{r_{out}^2}{4R_{out}^2} - \frac{r_{side}^2}{4R_{side}^2} - \frac{r_{long}^2}{4R_{long}^2} \right). \quad (3.11)$$

594 The main difference of this source function is that it has three different and inde-
 595 pendent widths R_{out} , R_{side} , R_{long} and they are defined in the LCMS, not in PRF.
 596 Unlike in PRF, in LCMS an equal-time approximation is not used. For identical
 597 particles this is not a problem - only Coulomb interaction inside a wave function
 598 depends on Δt .

599 Relationship between one-dimensional and three-dimensional source sizes

600 Up to now, most of femtoscopic measurements were limited only to averaged
 601 source size R_{av}^L (the letter “L” in superscript stands for LCMS):

$$S_{1D}^{LCMS}(\mathbf{r}) = \exp \left(-\frac{r_{out}^2 + r_{side}^2 + r_{long}^2}{2R_{av}^L} \right). \quad (3.12)$$

602 The relationship between between $S_{1D}^{LCMS}(\cdot)$ and $S_{3D}^{LCMS}(\cdot)$ is given by:

$$S_{3D}^{LCMS}(r) = \int \exp \left(-\frac{r_{out}^2}{2R_{out}^L} - \frac{r_{side}^2}{2R_{side}^L} - \frac{r_{long}^2}{2R_{long}^L} \right) \times \delta \left(r - \sqrt{r_{out}^2 + r_{side}^2 + r_{long}^2} \right) dr_{out} dr_{side} dr_{long}. \quad (3.13)$$

603 The one-dimensional source size corresponding to the three-dimensional one can
 604 be approximated by the following form:

$$S_{1D}^{LCMS}(r) = r^2 \exp \left(-\frac{r^2}{2R_{av}^L} \right). \quad (3.14)$$

605 The equation above assumes that $R_{out}^L = R_{side}^L = R_{long}^L$ hence $R_{av}^L = R_{out}^L$. If this
 606 condition is not satisfied, one can not give explicit mathematical relation between
 607 one-dimensional and three-dimensional source sizes. However, for realistic val-
 608 ues of R (i.e. for similar values of R_{out} , R_{side} , R_{long}), the S_{3D}^{LCMS} from Eq. 3.13 is
 609 not very different from Gaussian distribution and can be well approximated by
 610 Eq. 3.13.

611 A deformation of an averaged source function in case of big differences in
 612 R_{out} , R_{side} , R_{long} is presented in the Fig. 3.3. A three-dimensional Gaussian dis-
 613 tribution with varying widths was averaged into one-dimensional function using

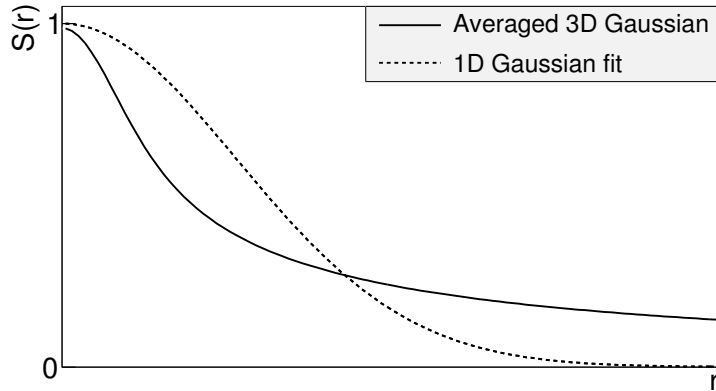


Figure 3.3: An averaged three-dimensional Gaussian source function with different widths was averaged into one-dimensional function. To illustrate deformations, one-dimensional Gaussian distribution was fitted.

the Eq. 3.13. Afterwards, an one-dimensional Gaussian distribution was fitted.
One can notice a heavy tail of an averaged distribution in long r region, which
makes an approximation using one-dimensional distribution in this case quite
inaccurate.

Using Eq. 3.13 and Eq. 3.14 one can obtain a relation between one-dimensional width and the three-dimensional ones. Through numerical calculations one can find the following approximate relation [25]:

$$R_{av}^L = \sqrt{\left(R_{out}^L\right)^2 + \left(R_{side}^L\right)^2 + \left(R_{long}^L\right)^2} / 3 . \quad (3.15)$$

This equation does not depend on the pair velocity, hence it is valid in the LCMS and PRF.

3.2.4 Theoretical correlation function

The fundamental object in a particle interferometry is a correlation function. The correlation function is defined as:

$$C(\mathbf{p}_a, \mathbf{p}_b) = \frac{P_2(\mathbf{p}_a, \mathbf{p}_b)}{P_1(\mathbf{p}_a)P_1(\mathbf{p}_b)} , \quad (3.16)$$

where P_2 is a conditional probability to observe a particle with momentum \mathbf{p}_b if particle with momentum \mathbf{p}_a was also observed. A P_1 is a probability to observe a particle with a given momentum. The relationship between source emission function, pair wave function and the correlation function is described by the following equation:

$$C(\mathbf{p}_1, \mathbf{p}_2) = \int S_{AB}(\mathbf{p}_1, \mathbf{x}_1, \mathbf{p}_2, \mathbf{x}_2) |\Psi_{AB}|^2 d^4\mathbf{x}_1 d^4\mathbf{x}_2 \quad (3.17)$$

Substituting the one-dimensional emission function (Eq. 3.10) into the integral above yields the following form of correlation function in PRF:

$$C(q) = 1 + \lambda \exp(-R_{inv}^2 q^2) \quad (3.18)$$

where q is a momentum difference between two particles. When using the three-dimensional emission function (Eq. 3.11) one gets the following correlation function defined in the LCMS:

$$C(\mathbf{q}) = 1 + \lambda \exp(-R_{out}^2 q_{out}^2 - R_{side}^2 q_{side}^2 - R_{long}^2 q_{long}^2) \quad (3.19)$$

where q_{out} , q_{side} , q_{long} are \mathbf{q} components in the outward, sideward and longitudinal direction. The λ parameter in the equations above determines correlation strength. The lambda parameter has values in the range $\lambda \in [-0.5, 1]$ and it depends on a pair type. In case of pairs of identical bosons (like $\pi\pi$ or KK) the lambda parameter $\lambda \rightarrow 1$. For identical fermions (e.g. $p-p$) $\lambda \rightarrow -0.5$. Values of λ observed experimentally are lower than 1 (for bosons) and greater than -0.5 (for fermions). There are few explanations to this effect: detector efficiencies, inclusion of misidentified particles in a used sample or inclusion of non-correlated pairs (when one or both particles come from e.g. long-lived resonance). The analysis carried out in this work uses data from a model, therefore the detector efficiency and particle purity is not taken into account [25].

3.2.5 Spherical harmonics decomposition of a correlation function

Results coming from an analysis using three-dimensional correlation function in Cartesian coordinates are quite difficult to visualize. To do that, one usually performs a projection into a one dimension in outward, sideward and longitudinal directions. One may loose important information about a correlation function in this procedure, because it gives only a limited view of the full three-dimensional structure. Recently, a more advanced way of presenting correlation function - a spherical harmonics decomposition, was proposed. The three-dimensional correlation function is decomposed into an infinite set of components in a form of one-dimensional histograms $C_l^m(q)$. In this form, a correlation function is defined as a sum of a series [26]:

$$C(\mathbf{q}) = \sum_{l,m} C_l^m(q) Y_l^m(\theta, \phi), \quad (3.20)$$

where $Y_l^m(\theta, \phi)$ is a spherical harmonic function. Spherical harmonics are an orthogonal set of solutions to the Laplace's equation in spherical coordinates. Hence, in this approach, a correlation function is defined as a function of q , θ and ϕ . To obtain C_l^m coefficients in the series, one has to calculate the following integral:

$$C_l^m(q) = \int_{\Omega} C(q, \theta, \phi) Y_l^m(\theta, \phi) d\Omega, \quad (3.21)$$

655 where Ω is a full solid angle.

Spherical harmonics representation has several important advantages. The main advantage of this decomposition is that it requires less statistics than traditional analysis performed in Cartesian coordinates. Another one is that it encodes full three-dimensional information in a set of one-dimensional plots. In principle it does not have to be an advantage, because full description of a correlation function requires infinite number of l, m components. But it so happens that the intrinsic symmetries of a pair distribution in a femtoscopic analysis result in most of the components to vanish. For the identical particles correlation functions, all coefficients with odd values of l and m disappear. It has also been shown, that the most significant portion of femtoscopic data is stored in the components with the lowest l values. It is expected that, the main femtoscopic information is contained in the following components [25]:

$$C_0^0 \rightarrow R_{LCMS}, \quad (3.22)$$

$$\Re C_2^0 \rightarrow \frac{R_T}{R_{long}}, \quad (3.23)$$

$$\Re C_2^2 \rightarrow \frac{R_{out}}{R_{side}}, \quad (3.24)$$

656 where $R_{LCMS} = \sqrt{(R_{out}^2 + R_{side}^2 + R_{long}^2)/3}$ and $R_T = \sqrt{(R_{out}^2 + R_{side}^2)/2}$.
 657 The C_0^0 is sensitive to the overall size of a correlation function. The $\Re C_2^0$ carries
 658 the information about the ratio of the transverse to the longitudinal radii, due
 659 to its $\cos^2(\theta)$ weighting in Y_2^0 . The component $\Re C_2^2$ with its $\cos^2(\phi)$ weighting
 660 encodes the ratio between outward and sideward radii. Thus, the spherical har-
 661 monics method allows to obtain and analyze full three-dimensional femtoscopic
 662 information from a correlation function [25].

663 3.3 Experimental approach

664 The correlation function is defined as a probability to observe two particles
 665 together divided by the product of probabilities to observe each of them sepa-
 666 rately (Eq. 3.16). Experimentally this is achieved by dividing two distributions
 667 of relative momentum of pairs of particles coming from the same event and the
 668 equivalent distribution of pairs where each particle is taken from different colli-
 669 sions. In this way, one obtains not only femtoscopic information but also all other
 670 event-wide correlations. This method is useful for experimentalists to estimate
 671 the magnitude of non-femtoscopic effects. There exists also a different approach,
 672 where two particles in pairs in the second distribution are also taken from the
 673 same event. The second method gives only information about physical effects
 674 accessible via femtoscopy. The aim of this work is a study of effects coming from
 675 two particle interferometry, hence the latter method was used.

676 In order to calculate experimental correlation function, one uses the follow-
 677 ing approach. One has to construct two histograms: the *numerator* N and the

678 denominator D with the particle pairs momenta, where particles are coming from
 679 the same event. Those histograms can be one-dimensional (as a function of $|\mathbf{q}|$),
 680 three dimensional (a function of three components of \mathbf{q} in LCMS) or a set of one-
 681 dimensional histogram representing components of the spherical harmonic de-
 682 composition of the distribution. The second histogram, D is filled for each pair
 683 with the weight 1.0 at a corresponding relative momentum $\mathbf{q} = 2\mathbf{k}^*$. The first one,
 684 N is filled with the same procedure, but the weight is calculated as $|\Psi_{ab}(\mathbf{r}^*, \mathbf{k}^*)|^2$.
 685 A division N/D gives the correlation function C . This procedure can be simply
 686 written as [25]:

$$C(\mathbf{k}^*) = \frac{N}{D} = \frac{\sum_{n_i \in D} \delta(\mathbf{k}^* i - \mathbf{k}^*) |\Psi_{ab}(\mathbf{r}^* i, \mathbf{k}^* i)|^2}{\sum_{n_i \in D} \delta(\mathbf{k}^* i - \mathbf{k}^*)} . \quad (3.25)$$

The D histogram represents the set of all particle pairs used in calculations.
 The n_i is a pair with the its relative momentum $\mathbf{k}^* i$ and relative separation $\mathbf{r}^* i$.
 The wave function used in Eq. 3.25 has one of the following forms:

$$|\Psi_{\pi\pi}(\mathbf{r}^*, \mathbf{k}^*)|^2 = |\Psi_{KK}(\mathbf{r}^*, \mathbf{k}^*)|^2 = 1 + \cos(2\mathbf{k}^*\mathbf{r}^*) , \quad (3.26)$$

$$|\Psi_{pp}(\mathbf{r}^*, \mathbf{k}^*)|^2 = 1 - \frac{1}{2} \cos(2\mathbf{k}^*\mathbf{r}^*) . \quad (3.27)$$

687 The first one is used in case of bosons, and the latter one is for identical fermi-
 688 ons. Mathematically, the procedure of calculating the Eq. 3.25 is equivalent to a
 689 calculation of an integral in Eq. 3.17 through a Monte-Carlo method.

690 3.4 Scaling of femtoscopic radii

691 In the hydrodynamic models describing expansion of a quark-gluon plasma,
 692 particles are emitted from the source elements. Each of the source elements is
 693 moving with the velocity u_μ given by hydrodynamic equations. Because solu-
 694 tions of those equations are smooth, nearby source elements have similar velo-
 695 cities. Each emitted particle from a certain source element is boosted with the
 696 flow velocity u_μ according to the point of origin. Hence particles emitted close
 697 to each other (pairs with large transverse momentum $|\mathbf{k}_T|$) will gain the similar
 698 velocity boost, they can combine into pairs with small relative momenta ($|\mathbf{q}|$) and
 699 therefore become correlated. If the two particles are emitted far away from each
 700 other (a pair with small $|\mathbf{k}_T|$), the flow field u_μ in their point of emission might
 701 be very different and it will be impossible for them to have sufficiently small rel-
 702 ative momenta in order to be in region of interference effect. This effect is visible
 703 in a width of a correlation function in the Fig. 3.4. The correlation function gets
 704 broader for greater values of $|\mathbf{k}_T|$ and the femtoscopic radius R becomes smal-
 705 ler [8, 27].

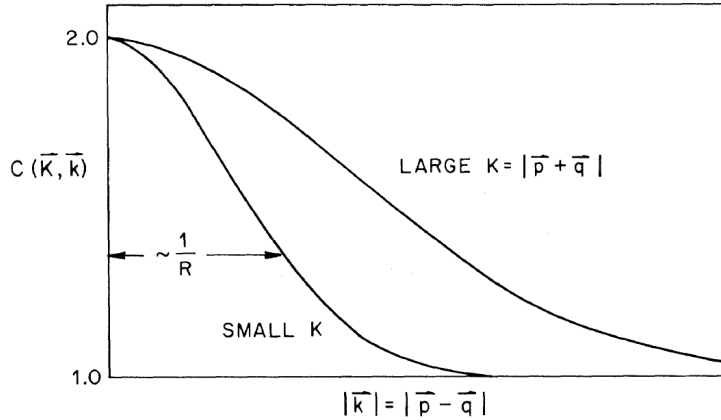


Figure 3.4: Correlation function width dependence on total pair momentum. Pion pairs with a large total momentum are more correlated [27].

706 3.4.1 Scaling in LCMS

Hydrodynamic calculations performed in LCMS show that femtoscopic radii in outward, sideward, and longitudinal direction show dependence on transverse mass $m_T = \sqrt{k_T^2 + m^2}$, where m is a mass of a particle [28]. Moreover, experimental results show that this scaling is observed for R_{LCMS} radii also. This dependence can be expressed as follows:

$$R_i = \alpha m_T^{-\beta} \quad (3.28)$$

707 where i subscript indicates that this equation applies to R_{out} , R_{side} and R_{long}
 708 radii. The β exponent is approximately equal 0.5. In case of strong transversal
 709 expansion of the emitting source, the decrease of longitudinal interferometry ra-
 710 dius can be more quick than $m_T^{-0.5}$, hence one can expect for longitudinal radii
 711 greater values of $\beta > 0.5$ [28].

712 3.4.2 Scaling in PRF

713 In the collisions at the LHC energies, pions are most abundant particles and
 714 their multiplicities are large enough to enable three-dimensional analysis. How-
 715 ever, for heavier particles, such as kaons and protons statistical limitations arise.
 716 Hence it is often possible to only measure one-dimensional radius R_{inv} for those
 717 particles. The R_{inv} is then calculated in the PRF. The transition from LCMS to
 718 PRF is a Lorentz boost in the direction of pair transverse momentum with velo-
 719 city $\beta_T = p_T/m_T$. Hence only R_{out} radius changes:

$$R_{out}^* = \gamma_T R_{out}. \quad (3.29)$$

720 The one-dimensional R_{inv} radius is direction-averaged source size in PRF. One
 721 can notice, that such power-law scaling of R_{inv} described by Eq. 3.28 is not

722 observed. To recover such scaling in PRF one has to take into consideration two
 723 effects when transforming variables from LCMS to PRF: overall radius growths
 724 and source distribution becomes non-Gaussian, while developing long-range
 725 tails (see Fig. 3.3 for an example). The interplay of these two effects can be
 726 accounted with an approximate formula:

$$R_{inv} = \sqrt{(R_{out}^2 \sqrt{\gamma_T} + R_{side}^2 + R_{long}^2)/3} . \quad (3.30)$$

Assuming that all radii are equal $R_{out} = R_{side} = R_{long}$ this formula can be simplified:

$$R_{LCMS} \approx R_{inv} \times [(\sqrt{\gamma_T} + 2)/3]^{-1/2} . \quad (3.31)$$

727 This approximate formula allows to restore power-law behaviour of the scaled
 728 radii not only when the radii are equal, but also when their differences are small
 729 (for explanation see the last part of the section 3.2.3).

730 This method of recovering scaling in PRF can be used as a tool for the search
 731 of hydrodynamic collectivity between pions, kaons and protons in heavy ion col-
 732 lisions with the measurement of one-dimensional radius in PRF.

733 **Chapter 4**

734 **Results**

735 For the purposes of the femtoscopy analysis in this thesis, the THERMINATOR
736 model was used to generate large number of events for eight different sets of
737 initial conditions corresponding the following centrality ranges: 0-5%, 0-10%, 10-
738 20%, 20-30%, 30-40%, 40-50%, 50-60% and 60-70% for the Pb-Pb collisions at the
739 centre of mass energy $\sqrt{s_{NN}} = 2.76 \text{ TeV}$.

740 **4.1 Identical particles correlations**

741 The correlation functions (three-dimensional and one-dimensional) were cal-
742 culated separately for the following different pairs of identical particles: π - π , K -
743 K and p - p for nine k_T bins (in GeV/c): 0.1-0.2, 0.2-0.3, 0.3-0.4, 0.4-0.5, 0.6-0.7,
744 0.7-0.8, 0.8-1.0 and 1.0-1.2. In case of kaons, k_T ranges start from 0.3 and for pi-
745 ons from 0.4 and for both of them the maximum value is 1.0. The k_T ranges for
746 the heavier particles were limited to maintain sufficient multiplicity to perform
747 reliable calculations.

748 **4.1.1 Spherical harmonics components**

749 The three-dimensional correlation function as a function of relative
750 momentum q_{LCMS} was calculated in a form of components of spherical
751 harmonics series accordingly to the Eq. 3.21. In the femtoscopy analysis of
752 identical particles, the most important information is stored in the $\Re C_0^0$, $\Re C_2^0$
753 and $\Re C_2^2$, hence only those components were analyzed. Correlation functions
754 obtained in this procedure were calculated for the different centrality bins for the
755 pairs of pions, kaons and protons. They are presented in the Fig. 4.1, 4.2 and 4.3.

756 Coefficients for pairs of identical bosons (pions and kaons) are shown in the
757 Fig. 4.1 and 4.2. The wave function symmetrization (Bose-Einstein statistics)
758 causes the increase of a correlation in the low relative momenta regime ($q_{LCMS} <$
759 0.06 GeV/c or even $q_{LCMS} < 0.12$ GeV/c for more peripheral collisions). It is
760 clearly visible in the $\Re C_0^0$ component. The $\Re C_0^0$ resembles one-dimensional cor-

relation function and in fact it encodes information about overall source radius. The second coefficient $\Re C_2^0$ differs from zero (is negative), which yields the information about the ratio R_T/R_{long} . The $\Re C_2^2$ stores the R_{out}/R_{side} ratio and one can notice that is non-vanishing (is also negative).

The correlation function for a pair of identical fermions is presented in the Fig. 4.3. An influence of wave function anti-symmetrization (Fermi-Dirac statistics) has its effect in the decrease of a correlation down to 0.5 at low relative momentum ($q_{LCMS} < 0.1 \text{ GeV/c}$ or $q_{LCMS} < 0.15 \text{ GeV/c}$ for more peripheral collisions), which can be observed in $\Re C_0^0$. The $\Re C_2^0$ and $\Re C_2^2$ coefficients differ from zero and are becoming positive.

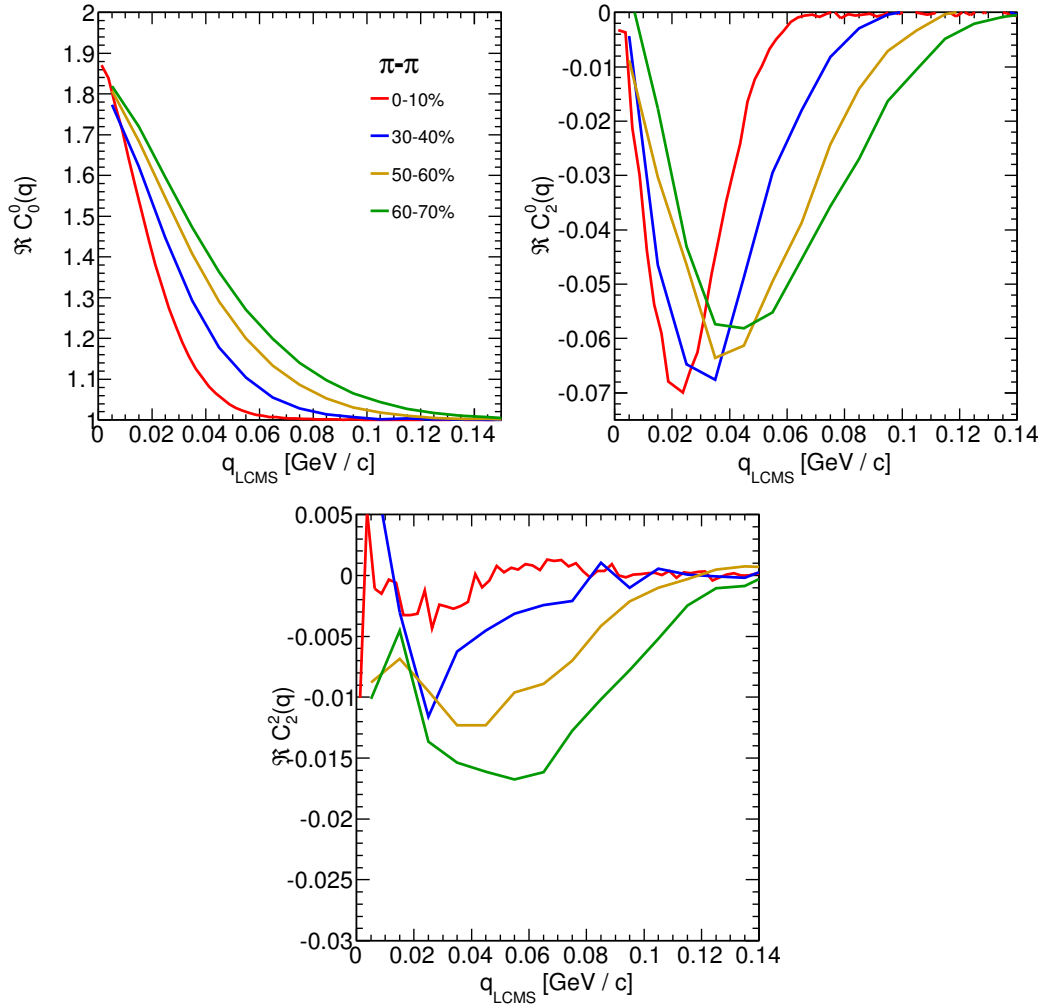


Figure 4.1: Spherical harmonics coefficients of the two-pion correlation function. From the top left: $\Re C_0^0$, $\Re C_2^0$ and $\Re C_2^2$. Only few centrality bins are presented for increased readability.

771 The common effect of the spherical harmonics form of a correlation function
 772 is the “mirroring” of the shape of the $\Re C_0^0$ coefficient - when correlation func-
 773 tion increases at low q_{LCMS} , the $\Re C_2^0$ and $\Re C_2^2$ are becoming negative and vice
 774 versa. This is quite different behaviour than in the case of correlations of non-
 775 identical particles, where the $\Re C_2^0$ still behaves in the same manner, but $\Re C_2^2$ has
 776 the opposite sign to the $\Re C_2^0$ [25].

777 In all cases, the correlation function gets wider with the peripherality of a
 778 collision i.e. the correlation function for most central collisions (0-10%) is much
 779 narrower than for the most peripheral ones (60-70%). This phenomena in clearly

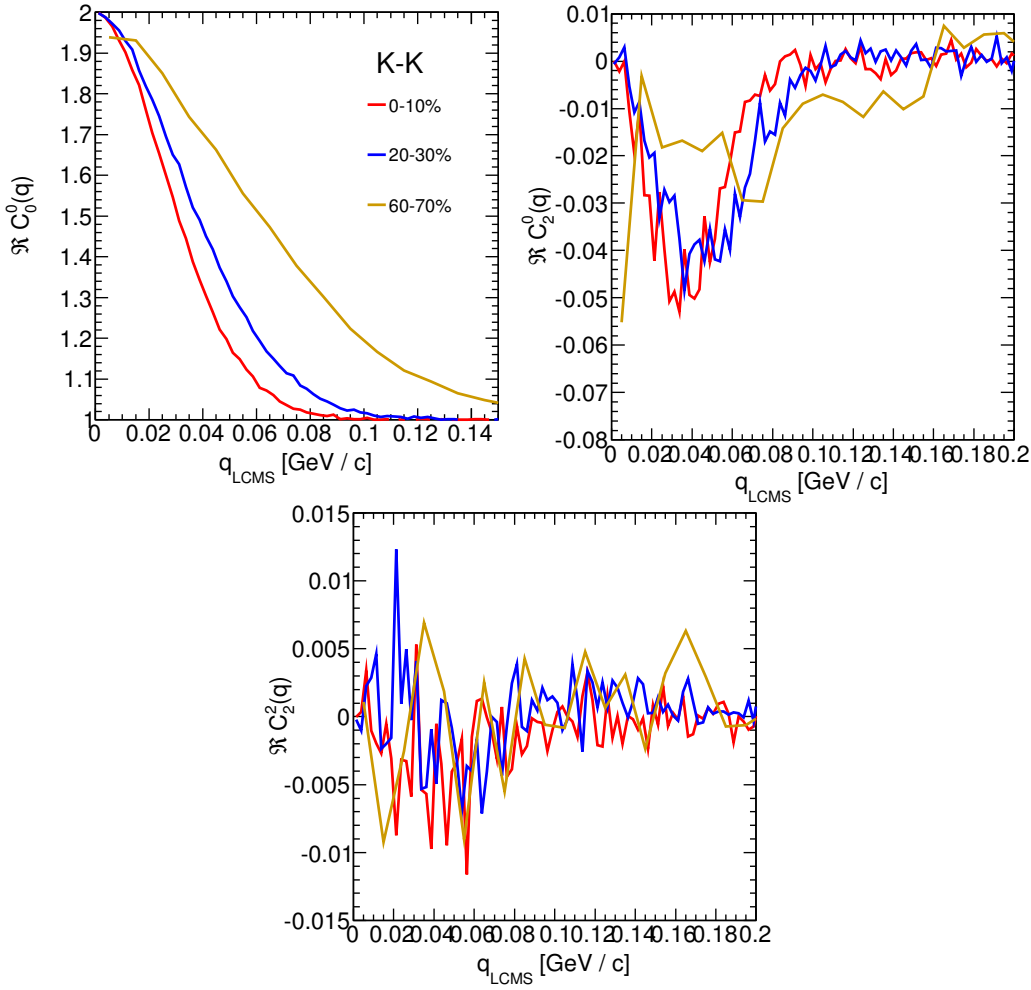


Figure 4.2: Spherical harmonics coefficients of the two-kaon correlation function. From the top left: $\Re C_0^0$, $\Re C_2^0$ and $\Re C_2^2$. Only few centrality bins are presented for increased readability. The $\Re C_2^2$ is noisy, but one can still notice that it differs from zero and is becoming negative.

visible the $\Re C_0^0$ coefficients. Other components are also affected by this effect, this is especially noticeable in the case of kaons and pions. For the protons, the results are noisy, hence this effect is not clearly distinguishable.

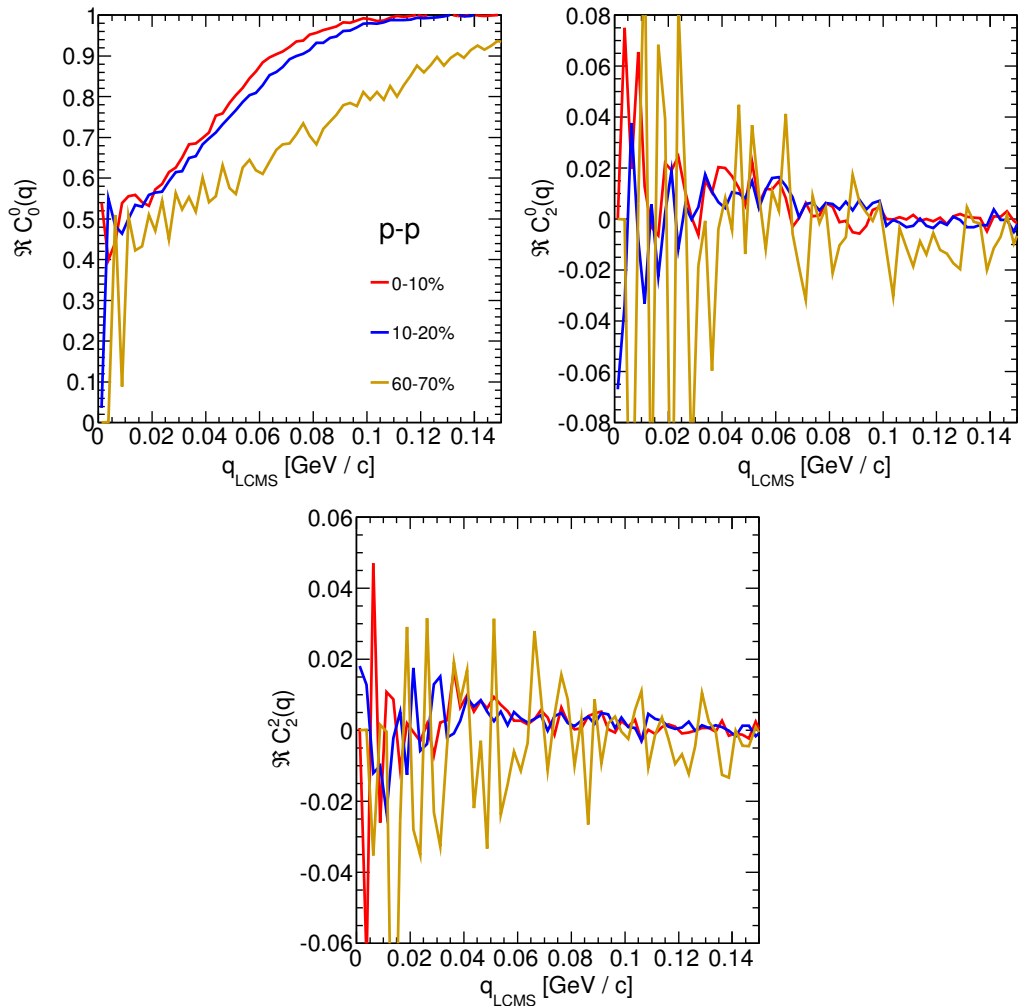


Figure 4.3: Spherical harmonics coefficients of the two-proton correlation function. From the top left: $\Re C_0^0$, $\Re C_2^0$ and $\Re C_2^2$. Only few centrality bins are presented for increased readability. The $\Re C_2^0$ and $\Re C_2^2$ are noisy, but one can still notice, that they differ from zero and are becoming positive.

783 **4.1.2 Centrality dependence of a correlation function**

784 The centrality dependence of a correlation function is especially visible in
 785 one-dimensional correlation functions. This effect is presented in the Fig. 4.4 -
 786 the correlation functions for pions, kaons and protons are plotted for the same
 787 k_T range but different centrality bins. One can notice that the width of a func-
 788 tion is smaller in the case of most central collisions. Hence, the femtoscopic radii
 789 (proportional to the inverse of width) are increasing with the centrality. An ex-
 790 planation for this growth is that in the most central collisions, a size of a created
 system is larger than for the peripheral ones.

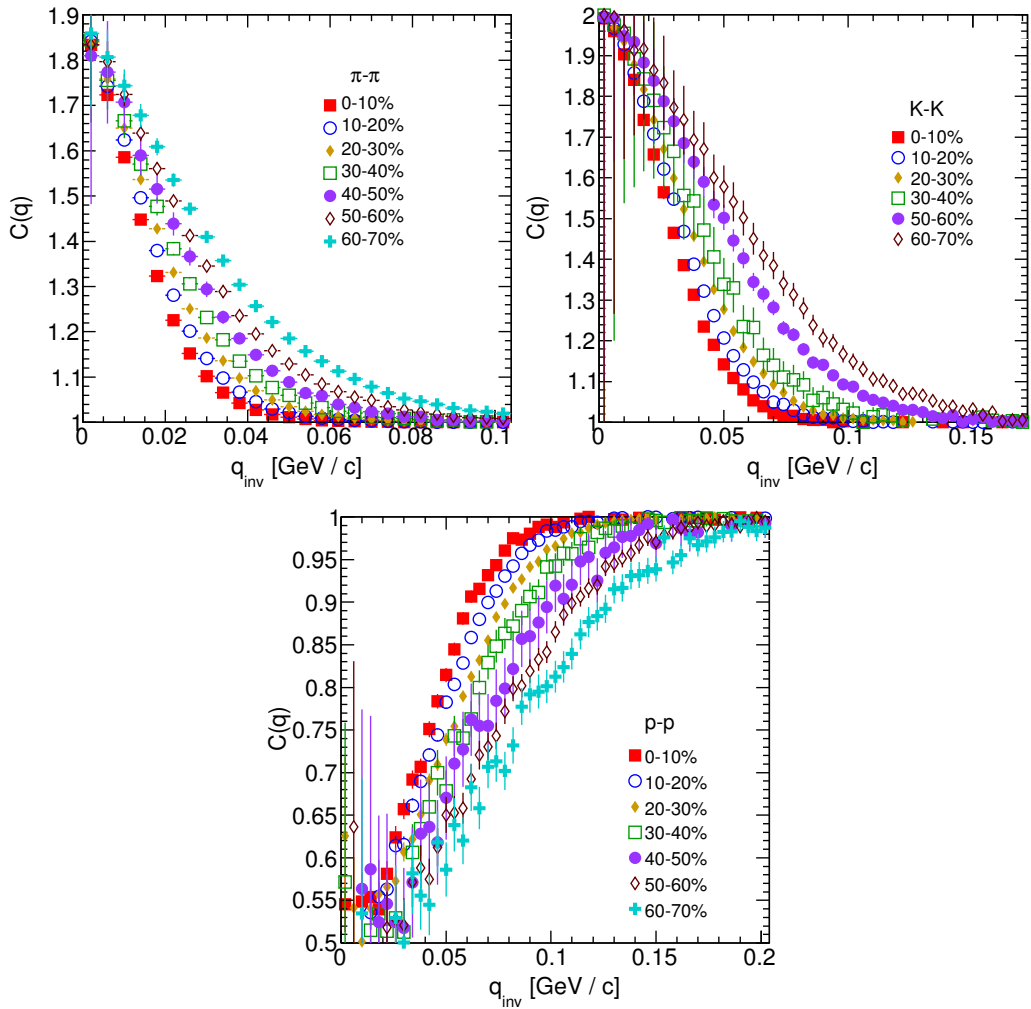


Figure 4.4: One-dimensional correlation function for pions (top left), kaons (top right) and protons (bottom) for different centralities.

792 **4.1.3 k_T dependence of a correlation function**

793 In the Fig. 4.5 there are presented one-dimensional correlation functions for
 794 pions, kaons and protons for the same centrality bin, but different k_T ranges. One
 795 can observe in all cases of the particle types, appearance of the same trend: with
 796 the increase of the total transverse momentum of a pair, the width of a correlation
 797 function increases and the femtoscopic radius decreases. The plots in the Fig. 4.5
 798 were zoomed in to show the influence of k_T .

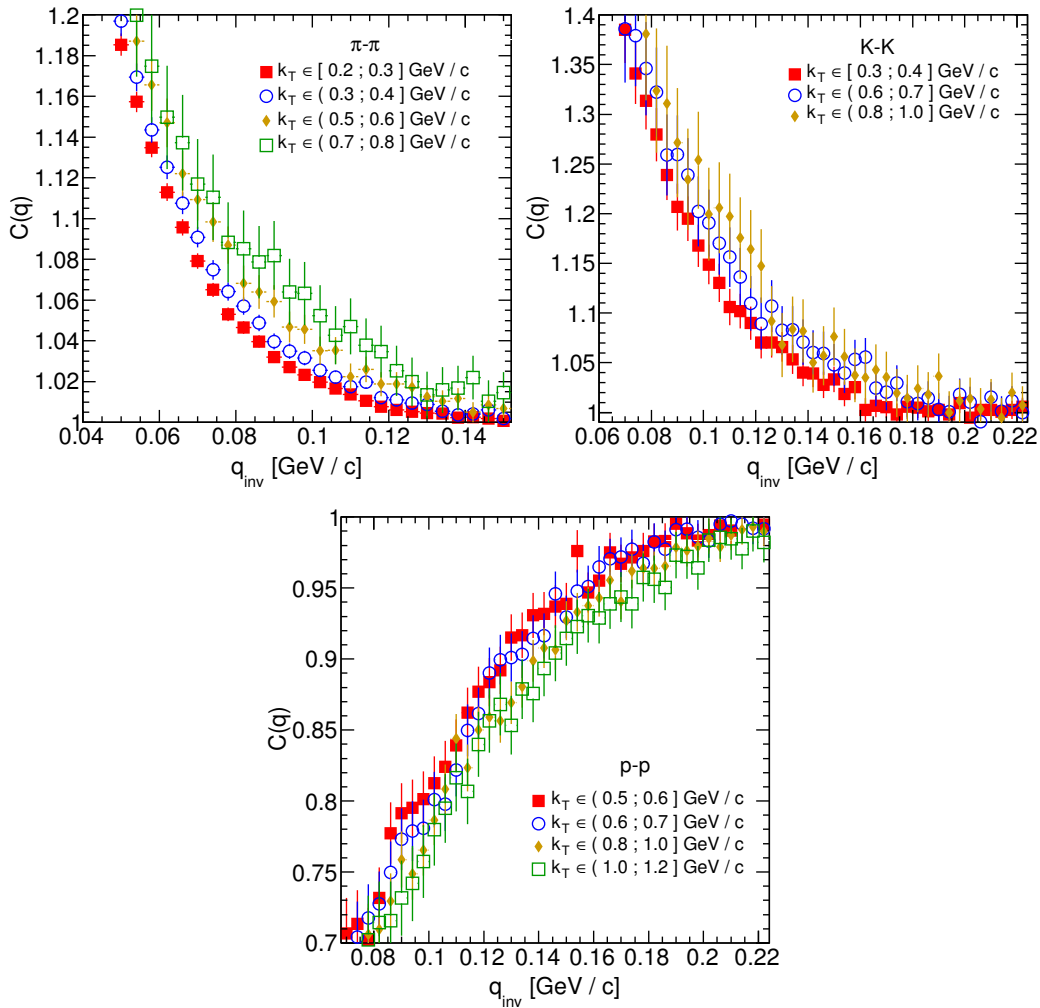


Figure 4.5: One-dimensional correlation functions for pions, kaons and protons, for the same centrality bin and different k_T ranges. The plot was zoomed in to the region which illustrates the k_T dependence in the best way. Only few of the calculated ranges are presented for better readability.

4.2 Results of the fitting procedure

In order to perform a quantitative analysis of a wide range of correlation functions, the theoretical formulas were fitted to the calculated experimental-like data. In this procedure, the femtoscopic radii for the three-dimensional as well as one-dimensional correlation functions were extracted. The main goal of this analysis is a verification of a common transverse mass scaling for different particles types. Obtained radii are plotted as a function of a transverse mass $m_T = \sqrt{k_T^2 + m^2}$. To test the scaling, the following power-law was fitted to the particular radii afterwards:

$$R_x = \alpha m_T^{-\beta}, \quad (4.1)$$

where the α and β are free parameters.

4.2.1 The three-dimensional femtoscopic radii scaling

In the Fig. 4.6 there are presented femtoscopic radii in the outward, sideward and longitudinal directions for the analysis of two-pion correlation functions in

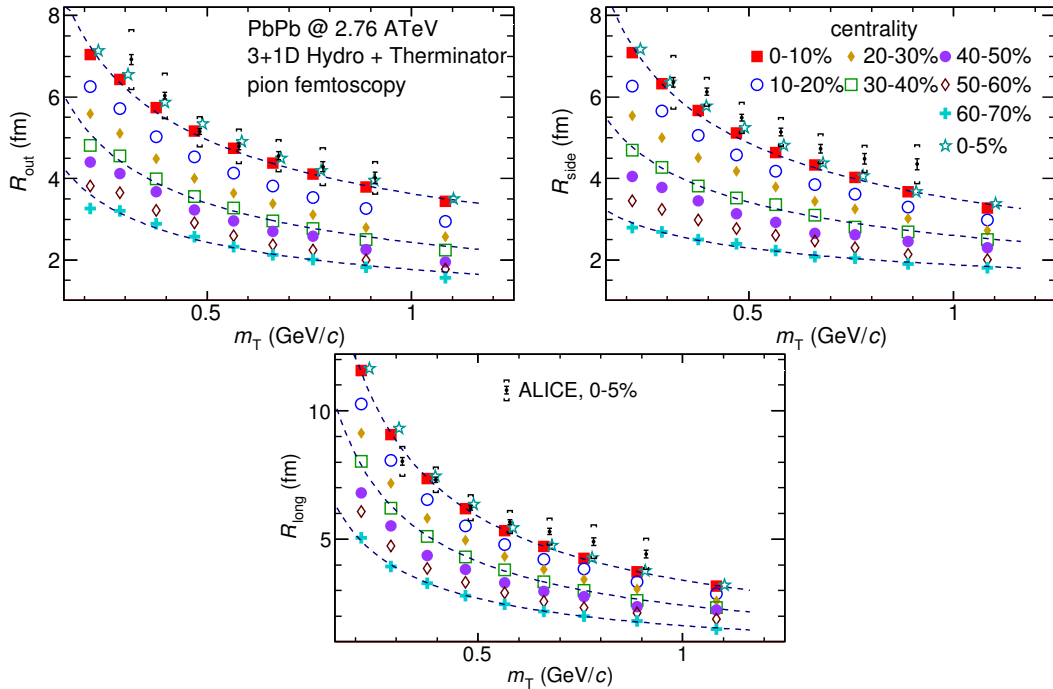


Figure 4.6: Femtoscopic radii in LCMS coming from two-pion correlation functions for all centrality bins as a function of m_T . The dashed lines are power-law fits. The most central collisions (0-5%) are compared to the results from ALICE [29]. The two datasets are shifted to the right for visibility [30].

the LCMS. The dashed lines are fits of the power law to the data. One can notice, that the power law describes well data points with a 5% accuracy. The β fit parameter for the outward direction is in the order of 0.45. For the sideward direction, this parameter has the similar value, but it is lower for the most peripheral collisions. In case of the longitudinal direction, the β has greater value, up to 0.75. In the Fig. 4.6 there are also compared results for the top 5% central collisions (star-shaped markers) with experimental data from ALICE [29]. The experimental results are consistent with the ones coming from the model predictions.

The Fig. 4.7 presents femtoscopic radii coming from the kaon calculations. The R_{out} , R_{side} and R_{long} fall also with the power-law within the 5% accuracy. The β parameter was larger in case of kaons: 0.59 in outward direction, 0.54 in the sideward and 0.86 for longitudinal.

The results for two-proton analysis are shown in the Fig. 4.8. The Eq. 4.1 was fitted to the data and tells that the protons also follow the m_T scaling within 5% range. The β parameter values were even bigger for the outward (0.58), sideward (0.61) and longitudinal (1.09) directions than for the other particle types.

The Fig. 4.9 presents results for the pions, kaons and protons together as a function of m_T . Considering differences in the β value for the fits for differ-

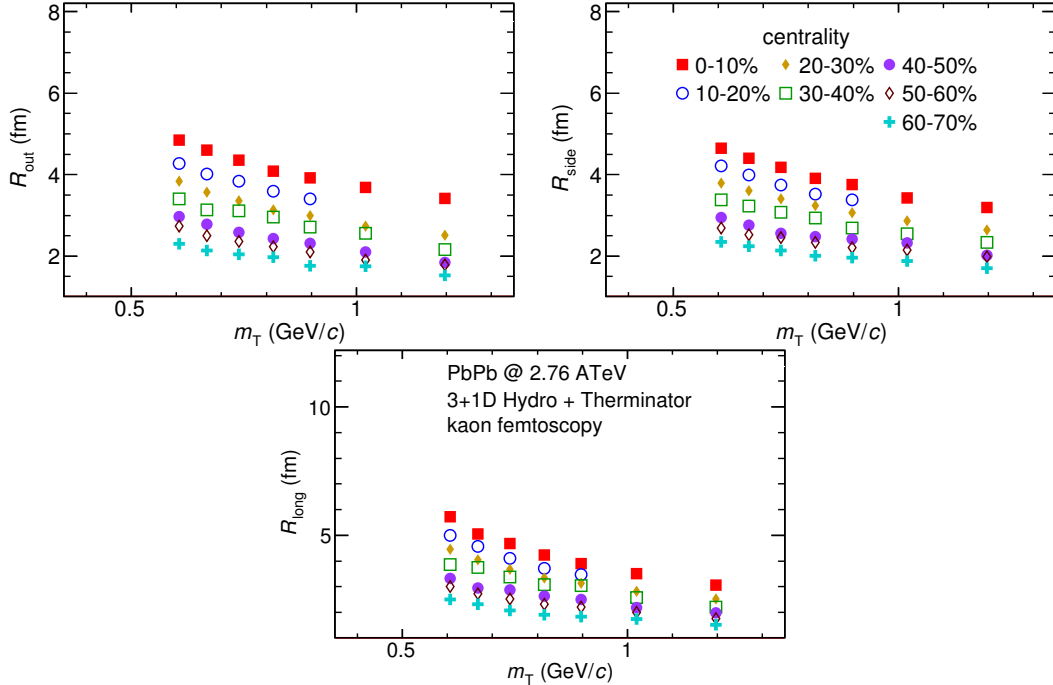


Figure 4.7: Femtoscopic radii extracted from two-kaon correlation functions for different centrality bins as a function of m_T . [30].

ent particles, one can suspect that there is no common scaling between different kinds of particles. However, when all of the results shown on the same plot, they are aligning on the common curve and the scaling is well preserved. The scaling accuracy is 3%, 5% and 4% for the 0-10%, 20-30% and 60-70% for the outward direction. For the sideward radii the scaling is better, with average deviations 2%, 2% and 3% respectively. In case of longitudinal direction the accuracy is 6%, 5% and 3% for the three centralities. The β parameter for the outward direction is close to the 0.42 in all cases. For the sideward direction it varies from 0.28 to 0.47 and is bigger for more central collisions. Regarding longitudinal radii, the exponent is bigger than the other two: $\beta \in [0.62; 0.72]$. Considering all results, the plotted radii are following the common power-law scaling within the 5% accuracy for all directions, centralities and particle types.

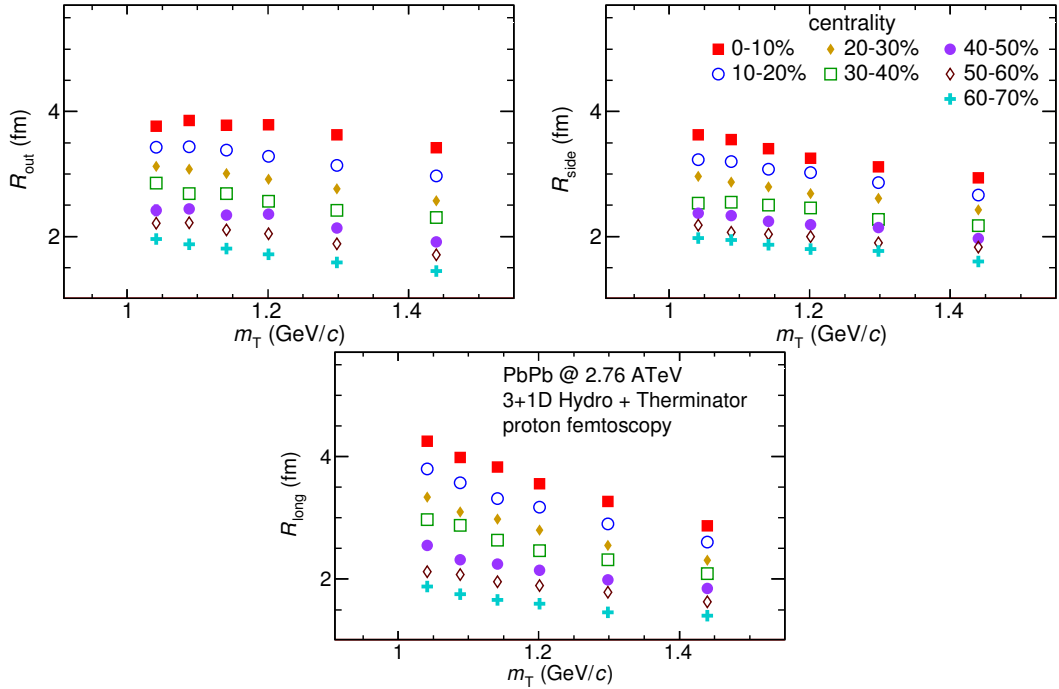


Figure 4.8: Femtoscopic radii extracted from two-proton correlation functions for different centrality bins as a function of m_T . [30].

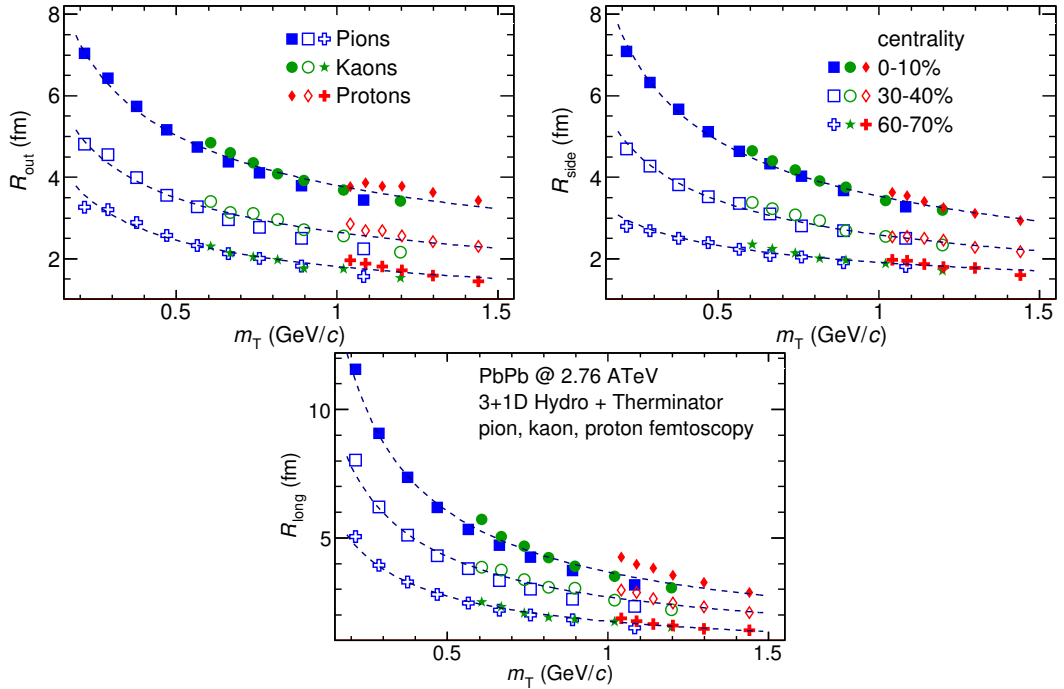


Figure 4.9: The results from the calculations for the pions, kaons and protons in for the three centralities presented on the common plot. One can notice that radii for particular centralities and different particle types follow the common power-law scaling. [30].

4.2.2 Scaling of one-dimensional radii

To the one-dimensional correlation function, the corresponding function in the PRF given by the Eq. 3.18 was fitted. The results from those fits are presented in the upper left plot in the Fig. 4.10. One immediately notices, that there is no common scaling of R_{inv} for different kind of particles. In the Fig. 4.9 the radii in the outward direction for the pions, kaons and protons for the same m_T are similar. However, when one performs a transition from the LCMS to the PRF, the R_{out} radius grows:

$$R_{out}^* = \gamma_T R_{out}, \quad (4.2)$$

where $\gamma_T = m_T/m$. For the lighter particles, the γ_T is much larger, hence the bigger growth of the R_{out} and the overall radius. This is visible in the Fig. 4.10 (top left), where the radii in the PRF for the lighter particles are bigger than for the heavier ones in case of the same m_T range.

In the Fig. 4.9 there is visible scaling in the outward, sideward and longitudinal direction. Hence one can expect an appearance of such scaling in a direction-averaged radius calculated in the LCMS. This radius is presented in the Fig. 4.10 (bottom) and indeed the R_{LCMS} exhibits power-law scaling with the m_T .

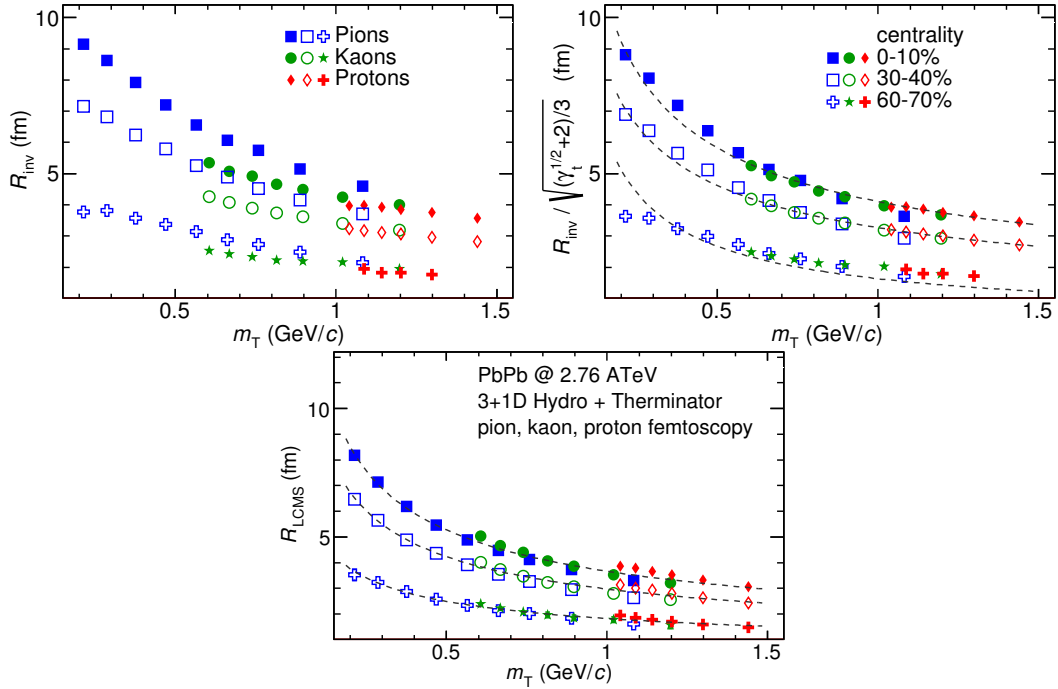


Figure 4.10: Top left: one-dimensional radius for pions, kaons and protons calculated in the PRF. Top right: the R_{inv} scaled by the proposed factor. Bottom: averaged one-dimensional radius in the LCMS for pions, kaons and protons. Only three centrality bins are shown for the better readability [30].

860 One can try to account the effect of an increase of the radii in the outward
 861 direction by using the appropriate scaling factor. In the Fig. 4.10 (top right) there
 862 are femtoscopic radii in the LCMS divided by the proposed scaling factor:

$$f = \sqrt{(\sqrt{\gamma_T} + 2)/3} . \quad (4.3)$$

863 The radii for pions, kaons and protons in the PRF after the division by f are
 864 following the power-law with the accuracy of 10%.

865 4.3 Discussion of the results

866 The femtoscopic radii obtained from the three-dimensional correlation func-
 867 tion fitting exhibit the m_T dependence described by the power law (Eq. 4.1). This
 868 scaling is preserved quite well with accuracy <10%. Observation of such scaling
 869 in a femtoscopic radii is a strong signal of appearance of a collective behaviour of
 870 a particle-emitting source created in the collision. The data used in the analysis
 871 was coming from the hydrodynamic model, hence one can indeed expect the
 872 appearance of this scaling. However, the results for pion femtoscopy from the
 873 ALICE at LHC are consistent with the data from analysis performed in this thesis
 874 (Fig. 4.6). This is a confirmation of an applicability of hydrodynamic models in a
 875 description of an evolution of a quark-gluon plasma.

876 The β parameter calculated in the fitting of the power-law to the femtoscopic
 877 radii is in the order of 0.5 in case of the radii in the transverse plane. This value is
 878 consistent with the hydrodynamic predictions. In case of longitudinal radii, the
 879 exponent is bigger (greater than 0.7), which is an indication of a strong transversal
 880 expansion in the system [28].

881 A scaling described above is visible in the LCMS, however due to limited stat-
 882 istics, analysis in this reference frame is not always possible. In such case one per-
 883 forms calculations in the PRF. The m_T scaling in the PRF is not observed - this has
 884 the trivial kinematic origin. A transition from the PRF to LCMS causes growth
 885 of the radius in the outward direction and the common power-law scaling for
 886 different particles breaks due to differences in the $\gamma_T(m_T)$ for different particle
 887 types. However one can try to deal with the radius growth and restore the scal-
 888 ing by multiplying the radii R_{inv} by an approximate factor $\sqrt{(\sqrt{\gamma_T} + 2)/3}$. The
 889 scaled R_{inv} are following the power-law and could be used as a verification of
 890 hydrodynamic behaviour in the investigated particle source.

891 The hadronic evolution and freeze-out in the THERMINATOR is followed
 892 by the resonance propagation and decay phase. A good accuracy of a scaling
 893 with the power-law indicated that the inclusion of the resonances does not
 894 break the m_T scaling. However, recent calculations including also hadron
 895 rescattering phase indicate that the scaling between pions and kaons is broken
 896 at the LHC [31].

Conclusions

This thesis presents the results of the two-particle femtoscopy of different particle kinds produced in Pb-Pb collisions at the centre of mass energy $\sqrt{s_{NN}} = 2.76$ TeV. The analysed data was generated by the THERMINATOR model using the (3+1)-dimensional hydrodynamic model.

The momentum correlations were studied for three different types of particle pairs: pions, kaons and protons. The data was analyzed for eight different sets of initial conditions corresponding the following centrality ranges: 0-5%, 0-10%, 10-20%, 20-30%, 30-40%, 40-50%, 50-60% and 60-70%. The correlation functions were calculated for the nine k_T bins from 0.1 GeV/c to 1.2 GeV/c. The calculations were performed using spherical harmonics decomposition of a three-dimensional correlation function. Using this approach, one can obtain full three-dimensional information about the source size using only the three coefficients: $\Re C_0^0$, $\Re C_2^0$ and $\Re C_2^2$. To perform further quantitative analysis, the femtoscopic radii were extracted through fitting.

The calculated correlation functions show expected increase of a correlation at low relative momenta in case of identical bosons (pions and kaons) and the decrease for the identical fermions (protons) respectively. This effect is especially visible in the first spherical harmonic coefficient $\Re C_0^0$. The other two components $\Re C_2^0$ and $\Re C_2^2$ are non-vanishing and are providing information about the ratios of radii in the outward, sideward and longitudinal directions.

An increase of width of a correlation function with the peripherality of a collision and the k_T is observed for pions, kaons and protons. This increase of femtoscopic radii (proportional to the inverse of width) with the k_T is related with the m_T scaling predicted by the hydrodynamic calculations.

Hydrodynamic equations are predicting appearance of femtoscopic radii common scaling for different kinds of particles with the $m_T^{-0.5}$ in the LCMS. In the results in this work, a common scaling for different particle types is observed in the LCMS in the outward, sideward and longitudinal direction. The direction-averaged radius R_{LCMS} also shows this power-law behaviour. The fitting of a power law $\alpha m_T^{-\beta}$ to the femtoscopic radii yielded the information, that the β exponent for the outward and sideward direction is in order of 0.5, which is consistent with the hydrodynamic predictions. For the longitudinal direction, the β is bigger (>0.7) than in the other directions which is an indication of a strong transverse flow. Femtoscopic radii in LCMS are following the

932 power-law scaling with the accuracy <5% for pions and kaons, and <10% in case
933 of protons.

934 In case of the one-dimensional radii R_{inv} calculated in the PRF, no common
935 scaling is observed. This is a consequence of a transition from the LCMS to the
936 PRF, which causes the growth of radius in the outward direction and breaks the
937 scaling for different particles. However, one can try to correct the influence of
938 the R_{out} growth with an approximate factor $\sqrt{(\sqrt{\gamma_T} + 2)/3}$. After the division
939 of the R_{inv} by the proposed factor, the scaling is restored with an accuracy <10%.
940 In this way, the experimentally simpler measure of the one-dimensional radii can
941 be used as a probe for the hydrodynamic collectivity.

942 The THERMINATOR model includes hydrodynamic expansion, statistical had-
943 ronization, resonance propagation and decay afterwards. The m_T scaling is pre-
944 dicted from the pure hydrodynamic calculations. However, this study shows,
945 that influence of the resonances on this scaling is less than 10%.

Bibliography

- [1] Standard Model of Elementary Particles - Wikipedia, the free encyclopedia
http://en.wikipedia.org/wiki/standard_model.
- [2] R. Aaij et al. (LHCb Collaboration). Observation of the resonant character of the $z(4430)^-$ state. *Phys. Rev. Lett.*, 112:222002, Jun 2014.
- [3] Donald H. Perkins. *Introduction to High Energy Physics*. Cambridge University Press, fourth edition, 2000. Cambridge Books Online.
- [4] G. Odyniec. *Phase Diagram of Quantum Chromo-Dynamics* - course at Faculty of Physics, Warsaw University of Technology, Jun 2012.
- [5] J. Beringer et al. (Particle Data Group). The Review of Particle Physics. *Phys. Rev.*, D86:010001, 2012.
- [6] Z. Fodor and S.D. Katz. The Phase diagram of quantum chromodynamics. 2009.
- [7] F. Karsch. Lattice results on QCD thermodynamics. *Nuclear Physics A*, 698(1-4):199 – 208, 2002.
- [8] Adam Kisiel. *Studies of non-identical meson-meson correlations at low relative velocities in relativistic heavy-ion collisions registered in the STAR experiment*. PhD thesis, Warsaw University of Technology, Aug 2004.
- [9] J. Bartke. *Relativistic Heavy Ion Physics*. World Scientific Pub., 2009.
- [10] W. Florkowski. *Phenomenology of Ultra-Relativistic Heavy-Ion Collisions*. World Scientific, 2010.
- [11] Science Grid This Week, October 25, 2006 - Probing the Perfect Liquid with the STAR Grid
http://www.interactions.org/sgtw/2006/1025/star_grid_more.html.
- [12] K. Grebieszkow. Fizyka zderzeń ciężkich jonów,
<http://www.if.pw.edu.pl/~kperl/hip/hip.html>.
- [13] Ulrich W. Heinz. From SPS to RHIC: Maurice and the CERN heavy-ion programme. *Phys. Scripta*, 78:028005, 2008.

- 974 [14] J. Adams et al. Identified particle distributions in pp and Au+Au collisions
975 at $s(\text{NN})^{**}(1/2) = 200 \text{ GeV}$. *Phys.Rev.Lett.*, 92:112301, 2004.
- 976 [15] G. David, R. Rapp, and Z. Xu. Electromagnetic Probes at RHIC-II. *Phys.Rept.*,
977 462:176–217, 2008.
- 978 [16] A. Marin et al. Dilepton measurements with CERES. *PoS*, CPOD07:034,
979 2007.
- 980 [17] J. Adams et al. Experimental and theoretical challenges in the search for the
981 quark gluon plasma: The STAR Collaboration’s critical assessment of the
982 evidence from RHIC collisions. *Nucl.Phys.*, A757:102–183, 2005.
- 983 [18] Adam Kisiel, Tomasz Taluc, Wojciech Broniowski, and Wojciech
984 Florkowski. THERMINATOR: THERMal heavy-IoN generATOR. *Comput.Phys.Commun.*, 174:669–687, 2006.
- 986 [19] Mikolaj Chojnacki, Adam Kisiel, Wojciech Florkowski, and Wojciech Bro-
987 niowski. THERMINATOR 2: THERMal heavy IoN generATOR 2. *Comput.Phys.Commun.*, 183:746–773, 2012.
- 989 [20] I. et al (BRAHMS Collaboration) Bearden. Charged meson rapidity distri-
990 butions in central Au + Au collisions at $\sqrt{s_{\text{NN}}} = 200 \text{ GeV}$. *Phys. Rev. Lett.*,
991 94:162301, Apr 2005.
- 992 [21] W. Israel and J.M. Stewart. Transient relativistic thermodynamics and kin-
993 etic theory. *Annals of Physics*, 118(2):341 – 372, 1979.
- 994 [22] Piotr Bożek. Flow and interferometry in (3 + 1)-dimensional viscous hydro-
995 dynamics. *Phys. Rev. C*, 85:034901, Mar 2012.
- 996 [23] K. Kovtun, P. D. T. Son, and A. O. Starinets. Viscosity in strongly interacting
997 quantum field theories from black hole physics. *Phys. Rev. Lett.*, 94:111601,
998 Mar 2005.
- 999 [24] Fred Cooper and Graham Frye. Single-particle distribution in the hydro-
1000 dynamic and statistical thermodynamic models of multiparticle production.
1001 *Phys. Rev. D*, 10:186–189, Jul 1974.
- 1002 [25] Adam Kisiel. Nonidentical-particle femtoscopy at $\sqrt{s_{\text{NN}}} = 200 \text{ GeV}$ in hy-
1003 drodynamics with statistical hadronization. *Phys. Rev. C*, 81:064906, Jun
1004 2010.
- 1005 [26] Adam Kisiel and David A. Brown. Efficient and robust calculation of femto-
1006 scopic correlation functions in spherical harmonics directly from the raw
1007 pairs measured in heavy-ion collisions. *Phys.Rev.*, C80:064911, 2009.
- 1008 [27] S. Pratt. Pion Interferometry for Exploding Sources. *Phys.Rev.Lett.*, 53:1219–
1009 1221, 1984.

- 1010 [28] S.V. Akkelin and Yu.M. Sinyukov. The HBT-interferometry of expanding
1011 inhomogeneous sources. *Z.Phys.*, C72:501–507, 1996.
- 1012 [29] K. Aamodt et al. Two-pion Bose-Einstein correlations in central Pb-Pb colli-
1013 sions at $\sqrt{s_{NN}} = 2.76$ TeV. *Phys.Lett.*, B696:328–337, 2011.
- 1014 [30] A. Kisiel, M. Galazyn, and P. Bozek. Pion, kaon, and proton femtoscopy in
1015 Pb-Pb collisions at $\sqrt{s_{NN}}=2.76$ TeV modeled in 3+1D hydrodynamics. 2014.
- 1016 [31] V.M. Shapoval, P. Braun-Munzinger, Iu.A. Karpenko, and Yu.M. Sinyukov.
1017 Femtoscopy correlations of kaons in $Pb + Pb$ collisions at LHC within hy-
1018 drokinetic model. 2014.

¹⁰¹⁹ List of Figures

1020	1.1	The Standard Model of elementary particles [1].	3
1021	1.2	A string break and a creation of a pair quark-anti-quark [4].	5
1022	1.3	The coupling parameter α_s dependence on four-momentum transfer Q^2 [5].	6
1023	1.4	The QCD potential for a pair quark-antiquark as a function of distance for different temperatures. A value of a potential decreases with the temperature [4].	6
1024	1.5	A number of degrees of freedom as a function of a temperature [7].	7
1025	1.6	Phase diagram coming from the Lattice QCD calculations [8].	8
1026	1.7	Left: stages of a heavy ion collision simulated in the UrQMD model. Right: schematic view of a heavy ion collision evolution [8].	9
1027	1.8	Overlapping region which is created in heavy ion collisions has an almond shape. Visible x-z plane is a <i>reaction plane</i> . The x-y plane is a <i>transverse plane</i> . The z is a direction of the beam [11].	11
1028	1.9	Cross-section of a heavy ion collision in a transverse plane. Ψ_R is an angle between transverse plane and the reaction plane. The b parameter is an <i>impact parameter</i> - a distance between centers of nuclei during a collision. An impact parameter is related with the centrality of a collision and a volume of the quark-gluon plasma [12].	12
1029	1.10	<i>Lower:</i> The elliptic flow v_2 follows the hydrodynamical predictions for an ideal fluid perfectly. Note that > 99% of all final hadrons have $p_T < 1.5 \text{ GeV}/c$. <i>Upper left:</i> The v_2 plotted versus transverse kinetic energy $KE_T = m_T - m_0 = \sqrt{p_T^2 + m_0^2} - m_0$. The v_2 follows different universal curves for mesons and baryons. <i>Upper right:</i> When scaled by the number of valence quarks, the v_2 follows the same universal curve for all hadrons and for all values of scaled transverse kinetic energy [13].	13
1030	1.11	Invariant yield of particles versus transverse mass $m_T = \sqrt{p_T^2 + m_0^2}$ for π^\pm , K^\pm , p and \bar{p} at mid-rapidity for p+p collisions (bottom) and Au+Au events from 70-80% (second bottom) to 0-5% (top) centrality [14].	14

1051	1.12 Thermal photons spectra for the central Au+Au collisions at $\sqrt{s_{NN}} = 200$ GeV at computed within different hydrodynamical models compared with the pQCD calculations (solid line) and experimental data from PHENIX (black dots) [15].	15
1055	1.13 Left: Invariant mass spectrum of e^+e^- pairs in Pb+Au collisions at 158A GeV compared to the sum coming from the hadron decays predictions. Right: The expectations coming from model calculations assuming a dropping of the ρ mass (blue) or a spread of the ρ width in the medium (red) [16].	16
1060	1.14 Azimuthal angle difference $\Delta\phi$ distributions for different colliding systems at $\sqrt{s_{NN}} = 200$ GeV. Transverse momentum cut: $p_T > 2$ GeV. For the Au+Au collisions the away-side jet is missing [17]. . .	17
1063	3.1 Bertsch-Pratt direction naming convention used in heavy ion collision.	23
1065	3.2 The pair wave function is a superposition of all possible states. In case of particle interferometry it includes two cases: particles with momenta p_1, p_2 registered by detectors A, B and p_1, p_2 registered by B, A respectively.	24
1069	3.3 An averaged three-dimensional Gaussian source function with different widths was averaged into one-dimensional function. To illustrate deformations, one-dimensional Gaussian distribution was fitted.	27
1073	3.4 Correlation function width dependence on total pair momentum. Pion pairs with a large total momentum are more correlated [27]. .	31
1075	4.1 Spherical harmonics coefficients of the two-pion correlation function. From the top left: $\Re C_0^0$, $\Re C_2^0$ and $\Re C_2^2$. Only few centrality bins are presented for increased readability.	34
1078	4.2 Spherical harmonics coefficients of the two-kaon correlation function. From the top left: $\Re C_0^0$, $\Re C_2^0$ and $\Re C_2^2$. Only few centrality bins are presented for increased readability. The $\Re C_2^2$ is noisy, but one can still notice that it differs from zero and is becoming negative.	35
1082	4.3 Spherical harmonics coefficients of the two-proton correlation function. From the top left: $\Re C_0^0$, $\Re C_2^0$ and $\Re C_2^2$. Only few centrality bins are presented for increased readability. The $\Re C_2^0$ and $\Re C_2^2$ are noisy, but one can still notice, that they differ from zero and are becoming positive.	36
1087	4.4 One-dimensional correlation function for pions (top left), kaons (top right) and protons (bottom) for different centralities.	37

1089	4.5	One-dimensional correlation functions for pions, kaons and protons, for the same centrality bin and different k_T ranges. The plot was zoomed in to the region which illustrates the k_T dependence in the best way. Only few of the calculated ranges are presented for better readability.	38
1090	4.6	Femtoscopic radii in LCMS coming from two-pion correlation functions for all centrality bins as a function of m_T . The dashed lines are power-law fits. The most central collisions (0-5%) are compared to the results from ALICE [29]. The two datasets are shifted to the right for visibility [30].	39
1091	4.7	Femtoscopic radii extracted from two-kaon correlation functions for different centrality bins as a function of m_T . [30].	40
1092	4.8	Femtoscopic radii extracted from two-proton correlation functions for different centrality bins as a function of m_T . [30].	41
1093	4.9	The results from the calculations for the pions, kaons and protons in for the three centralities presented on the common plot. One can notice that radii for particular centralities and different particle types follow the common power-law scaling. [30].	42
1094	4.10	Top left: one-dimensional radius for pions, kaons and protons calculated in the PRF. Top right: the R_{inv} scaled by the proposed factor. Bottom: averaged one-dimensional radius in the LCMS for pions, kaons and protons. Only three centrality bins are shown for the better readability [30].	43
1095			
1096			
1097			
1098			
1099			
1100			
1101			
1102			
1103			
1104			
1105			
1106			
1107			
1108			
1109			
1110			
1111			